Impact of an isolated open water storm on sea ice and ocean conditions in the Arctic Ocean

Emma Bent[1], **Camille Lique**[1], **Peter Sutherland**[1]

[1]Univ. Brest, CNRS, Ifremer, IRD, Laboratoire d'Océanographie Physique et Spatiale (LOPS), IUEM, F29280 Plouzané, France

Key Points:

- Isolated open water wind storms delay the fall freeze-up due to a deepening of the mixed layer which increases the mixed layer heat content.
- Storm induced thick mixed layers isolate the sea ice from heat flux at the base of the mixed layer: ice can grow thicker.
- The ocean retains signatures of open water wind storms over the fall and winter seasons.

Corresponding author: Emma Bent, `emma.bent@ifremer.fr`

Abstract

Storms can have a direct impact on sea ice, but whether their effect is seen weeks to months later has received little attention. The immediate and longer term impacts of an idealized open water wind storm are investigated with a one-dimensional coupled ice-ocean model. Storms with different momentum, duration and date of occurrence are tested. During the storm, the mechanical forcing causes a deepening of the mixed layer, leading to an increase in mixed layer heat content, despite a decrease in mixed layer temperature. This results in a delay in sea ice formation that ranges between a few hours to weeks compared to the control run, depending on the storm characteristics. Throughout the freezing period, the storm-induced thick mixed layer experiences little variability, preventing warm water entrainment at the base of the mixed layer. This leads to faster sea ice growth compared to the control run, resulting in sea ice thickness differences of a few millimeters to around 10 cm before the melting onset. These results are stronger for runs with higher momentum storms which cause greater mixed layer deepening. Storms occurring in early August, when the ocean surface heat flux is positive, also amplify the results by forcing a greater increase in mixed layer heat content. The impacts of the storms are sensitive to the initial stratification, and amplified for a highly stratified ocean. We suggest that localized storms could significantly influence the seasonal dynamics of the mixed layer and consequently impact sea ice conditions.

Plain Language Summary

We use a numerical model to simulate a summer wind storm passing over an ice-free ocean, in order to study the immediate and longer term impacts on the ocean, as well as on sea ice formation and its evolution in winter. Results are compared to a situation without a storm. We find that the amount of heat in the surface layer of the ocean increases when the storm thickens the surface layer. This causes sea ice to form a few hours to weeks later compared to the situation without a storm. During fall and winter, sea ice is isolated from the heat stored in deeper layers of the ocean, again due to the thickening of the surface layer by the storm. Ice therefore grows thicker, leading to thickness differences at the end of winter ranging from a few millimeters to around 10 cm compared to the situation without a storm. Sea ice forms even later and grows faster when the storm is strong and occurs in early summer. Our study suggests that storms could be in part responsible for seasonal evolution of the surface layer of the ocean, which in turn has an impact on the sea ice conditions.

1 Introduction

The Arctic region is undergoing strong and rapid changes. One of the most striking changes is the melt of sea ice. Sea ice extent and thickness have been decreasing over the past four decades, a trend that has been observable with the advent of satellite observations (e.g., Stroeve et al., 2012; Kwok, 2018). According to CMIP6 projections (Notz & Community, 2020), the Arctic Ocean will likely experience the first sea-ice free months of September by the mid-21st century. The historically ice-covered Arctic Ocean is thus shifting towards an open ocean in summer, with significant consequences for the dynamics of the ocean, the air-sea exchanges, and the evolution of sea ice.

The loss of sea ice increases the open ocean area exposed to storms in summer and fall, and yields larger fetch, so that higher and more energetic wave fields are expected to develop in the Arctic Ocean (Thomson & Rogers, 2014). Wind and waves force the surface of the ocean, inducing mixing and increased air-sea fluxes (Thomson et al., 2022). As a consequence, the mixed layer can deepen (e.g., Dohan & Davis, 2011) and experience temperature and salinity changes. For instance, in July 2008 in the Beaufort Sea, Long and Perrie (2012) documented a 2°C cooling of the surface temperature due to enhanced mixing generated by a 4-day storm at 15 m/s. Storm induced mixing can also favor the release of heat stored below the mixed layer, which is a peculiarity of the Arctic stratification (e.g., Toole et al., 2010; Jackson et al., 2010). For example, Smith et al. (2018) examined the impact over 3 days of a strong wind and wave event (respectively up to 20 m/s and greater than 4 m), in the Beaufort Sea in October 2015. They observed that the wind-induced mixing released a significant amount of upper-ocean-stored heat (10 MJ.m^{-2}) that allowed for the melting of the pancake ice formed prior the event (as the storm occurred during the freezing period).

Numerous studies have looked at the local and short term impacts of strong wind and/or wave forcing on sea ice (e.g., Stopa et al., 2016; Boutin et al., 2020; Asplin et al., 2012, 2014; Collins et al., 2015), but whether these events can have a longer term impact on sea ice and affect its seasonal evolution has received little attention. Only Screen et al. (2011) established that there is a relationship between the number of late spring/early summer storms and the September sea ice conditions, as a low cyclone activity in spring could precondition the melting season and lead to reduced sea ice. Their study highlighted the potential for spring/summer storms to have a longer-term effect throughout the melting season.

To our knowledge, the processes responsible for affecting sea ice evolution in fall and winter, months after the passage of a summer storm, have not been described yet. Here, we focus on the following two questions: 1) How are the properties of the mixed layer modified during a storm and what are the relative contributions of mechanical and buoyancy forcing to these changes? 2) What are the impacts of a storm on the ocean and sea ice evolution on seasonal time scale?

To answer these questions, we simulate the effect of a wind event passing by over open water at the end of summer/beginning of fall in the Canadian Basin. We quantify the immediate impacts of the wind storm on the water column, as well as the longer term impacts on the water column and sea ice conditions. To that aim, we use a one-dimensional coupled ice-ocean model, with a parametrization of the effect of waves, to which we apply the forcing representing a set of idealized storms with varying intensity, duration, and date.

This paper is organized as follows. In section 2 we describe the set up of the one-dimensional model and the architecture of the model experiments. The results for the experiments are presented in section 3 to 6, with a focus on the storm impacts on mixed layer and sea ice properties (section 3), on the modulation of the timing (section 4) and efficiency of the sea ice formation (section 5). The mechanical and buoyancy forcing dur-

ing the storm are studied in section 6. Section 7 presents a sensitivity analysis to a different initial condition, in order to assess the role of ocean preconditioning. Conclusions are given in section 8.

2 Methods

2.1 Model description

We use the one-dimensional vertical configuration of the numerical model NEMO (G. Madec and the NEMO System Team, 2019), hereafter called NEMO1D, coupled with the sea ice model SI^3 (NEMO Sea Ice Working Group, 2019). The model is based on the 3D primitive equations (Reffray et al., 2015), with some simplifications to represent one-dimensional water column dynamics. There is no representation of horizontal advection (in the ocean and sea ice components) and no lateral mixing for tracers and dynamics, as there are no horizontal gradients. We only consider the vertical coordinate and time as independent coordinates in the primitive equations. The model is governed by 1D-approximated Reynolds averaged Navier-Stokes equations (RANS; equation 29a in Reffray et al., 2015), transport equations for temperature and salinity (equations 29b-c in Reffray et al., 2015), and a nonlinear equation of state for sea water (EOS-80; Fofonoff & Millard Jr, 1983) to calculate density.

We use a turbulent kinetic energy (TKE) turbulent closure scheme (Blanke & Delecluse, 1993) to parameterize the nonlinear vertical terms of the RANS equations. The TKE $\overline{e}$ is defined as:

$$\overline{e} = \frac{1}{2}\left(\overline{u'^2} + \overline{v'^2} + \overline{w'^2}\right), \tag{1}$$

where u', v' and w' are the fluctuation components of the Eulerian velocity vector $\mathbf{u} = (u, v, w)$. Variables are separated by Reynolds decompostion into mean and fluctuating components, represented with overbars and primes, respectively. The evolution of TKE is computed according to Blanke and Delecluse (1993) to which a source term is added to represent the effect of Langmuir circulation (LC; Axell, 2002). This evolution can be written as:

$$\frac{\partial \overline{e}}{\partial t} = \underbrace{-\overline{\mathbf{u}_h' w'} \cdot \frac{\partial \overline{\mathbf{u}_h}}{\partial z}}_{1} + \underbrace{\overline{w'b'}}_{2} \underbrace{- \frac{\partial}{\partial z}\left\{\overline{w'\overline{e}} + \frac{1}{\rho_0}\overline{w'p'}\right\}}_{3} - \underbrace{\epsilon}_{4} + \underbrace{P_{\mathrm{LC}}}_{5}, \tag{2}$$

with t the time, $\mathbf{u}_h = (u, v)$, b' the turbulent buoyancy fluctuation (defined as $b' = -g\rho'/\rho_0$, with $g = 9.81$ m.s^{-2} the gravitational acceleration and ρ' the density fluctuation), ρ_0 the background density, p' the turbulent pressure fluctuation, ϵ the dissipation, and P_{LC} the TKE source term due to LC defined below. Term 1 is the wind-forced production of TKE, term 2 is the buoyancy-forced production of TKE (heat and freshwater fluxes from the atmosphere and sea ice), term 3 is the vertical transport of TKE due to pressure diffusion and turbulent transport, term 4 is the dissipation of TKE, term 5 is the wave-forced production of TKE (generated by wave forcing at the ocean surface).

Surface wave breaking is parameterized through an additional term in the surface TKE boundary condition which is defined as a function of the surface stress and the wave age. It is also taken into account as part as the turbulent length scale boundary condition which is defined as a function of the surface stress (Craig & Banner, 1994; Mellor & Blumberg, 2004). The LC parametrization used to estimate term 5 in equation 2 is an analogy of the characteristic convective velocity scale (e.g., D'Alessio et al., 1998). Term 5 is given as: $P_{\mathrm{LC}}(z) = w_{\mathrm{LC}}^3(z)/H_{\mathrm{LC}}$, with w_{LC} the vertical velocity profile of LC and H_{LC} the LC depth. The latter is defined as the maximum depth a water parcel with

kinetic energy due to Stokes drift can reach, by converting its kinetic energy into potential energy. H_{LC} is often close to the mixed layer depth. w_{LC} is represented by a sine function which is a first-order approximation of the Langmuir cell structure:

$$w_{\mathrm{LC}} = \begin{cases} c_{\mathrm{LC}} |u_{\mathrm{SD}_0}| \sin(-\pi z / H_{\mathrm{LC}}) & \text{if } 0 \leq z \leq H_{\mathrm{LC}} \\ 0 & \text{otherwise} \end{cases}, \tag{3}$$

with c_{LC} a constant introduced by Axell (2002) and u_{SD_0} the surface Stokes drift. c_{LC} is typically chosen between 0.15 and 0.54 as suggested by Axell (2002). We choose $c_{\mathrm{LC}} = 0.30$ following the recommendation made by Couvelard et al. (2020) to obtain a better representation of the mixed later depth. The surface Stokes drift is parameterized as $u_{\mathrm{SD}_0} = 0.016\, U_{10}$ (Li & Garrett, 1993), with ${U_{10}}^2 = |\boldsymbol{\tau}|/(\rho_a C_D)$, the 10-m wind speed, and with $\boldsymbol{\tau} = (1-\lambda)\boldsymbol{\tau_a} + \lambda \boldsymbol{\tau_i}$, the ocean surface stress. $\boldsymbol{\tau_a}$ is the wind-driven component, $\boldsymbol{\tau_i}$ the ice-driven component and λ the sea ice concentration. Assuming the air density to be $\rho_a = 1.22$ kg/m^3 and the drag coefficient $C_D = 1.5 \times 10^{-3}$, the surface Stokes drift can be expressed as: $u_{\mathrm{SD}_0} = 0.377 |\boldsymbol{\tau}|^{1/2}$ (G. Madec and the NEMO System Team, 2019). Note that the drag coefficient is taken as a constant for the parametrization of the surface Stokes drift, although it varies with sea ice conditions for other NEMO1D calculations. As sea ice tends to attenuate waves and prevent the formation of LC (e.g., Wadhams et al., 1988), term 5 in equation 2 is set to zero for sea ice concentration above 25% and is scaled by the concentrations for value ranging between 0 and 25%. A sensitivity analysis for the numerics and parametrizations used in the configuration is provided in Supplementary Information.

2.2 Experimental design

2.2.1 Reference run

Our NEMO1D configuration is set up at the position of the Beaufort Gyre Exploration Project mooring A (referred to hereafter as BGEPA; Figure 1a), located at 75°N and 150°W in the seasonal ice zone (e.g., Proshutinsky et al., 2009). This location is close to the center of the Beaufort Gyre where the currents are weak (e.g., Regan et al., 2019), meaning that the advection terms that are not represented in our 1D model are expected to be small. We consider the top 500 m of the water column to include the surface layers affected by the wind and wave forcing. We choose a 1-m resolution in order to have a sufficient number of levels in the mixed layer.

The reference run is initialized with the mean of four Conductivity-Temperature-Depth (CTD) casts located within 1° of latitude and 3.3° of longitude of the BGEPA mooring, collected in August 2013 as part of the BGEP annual cruise. The mean profile has a 13.5-m thick mixed layer (Figure 1b,c) with a temperature of -1.2°C and a salinity of 26.4 psu. We define the mixed layer depth h as the shallowest depth at which the salinity is more than 0.1 psu greater than the surface salinity (Lemke & Manley, 1984). We use this definition rather than a definition based on density as it tends to capture the mixed layer depth more accurately than criteria proposed by previous studies (e.g., de Boyer Montégut et al., 2004; Peralta-Ferriz & Woodgate, 2015). The goal is to initialize our runs with a typical summer mixed layer of the Canadian basin where mixed layer depths usually range between 8-20 m (Peralta-Ferriz & Woodgate, 2015). At this season, the salinity profile is strongly stratified below the mixed layer. At 21-m depth is a near surface temperature maximum (NSTM) of -1°C. The latter forms when surface waters are heated during summer and are trapped beneath the colder mixed layer in winter (Jackson et al., 2010). At approximately 41-m depth is a temperature minimum of -1.2°C, which corresponds to the remnant of the winter mixed layer, overlying another local temperature maximum of 0.1°C called the Pacific Summer Water (PSW), which

originates from the Chukchi Sea (Jackson et al., 2010). We run the simulations from August 1 to June 30 (total of 11 months) to cover the open water and freezing periods.

We use climatological seasonal forcing in order to simulate an average year, representative of the 2005-2015 period. The climatological atmospheric forcing is obtained from the latest version of the Drakkar Forcing Set (version 5.2 built from ERA-I reanalysis data; Dussin et al., 2016). At the BGEPA position, we calculate the 2005-2015 daily climatologies for the 2-m air temperature and humidity, as well as the downward shortwave and longwave radiation at the sea surface. The latter are then smoothed with a 21-day centered moving average in order to remove the higher frequency variability (Figure 1d). We set the rain and snow forcings as constants (yearly means of the 2005-2015 climatology): 6.5×10^{-6} kg.m^{-2}.s^{-1} for rain and 3.3×10^{-6} kg.m^{-2}.s^{-1} for snow. The simulation is initialized with no sea ice. For the reference run, we set the wind speed as constant to 4 m/s, which is representative of the mean winds observed over the Arctic (Lindsay et al., 2014).

2.2.2 Sensitivity to wind storms

Our objective is to test the sensitivity of the mixed layer and sea ice conditions to wind anomalies, representing open water storms passing by the BGEPA mooring in summer or fall. We perform a large number of runs (245 in total), hereafter referred to as the '1D ensemble'. Only the wind forcing is modified from run to run. It remains constant throughout the runs, with a background value of 4 m/s, similar to the reference run, except for a specific period during which we apply a wind anomaly, that we refer to as 'storm' throughout the study. Then, the wind forcing increases instantly, following a rectangular window function shape (Figure 1e).

We test the sensitivity to a number of absolute magnitudes (6, 9, 12, 15, 18, 21 or 24 m/s), durations (3, 6, 12, 24, 48, 96 or 192 hours), and dates of storm ranging between August 1 and October 1 with two week intervals (i.e. 5 different dates). Figure 1e shows the wind forcing corresponding to a 4-day storm starting on September 1 with a 15 m/s magnitude. From the duration and magnitude, we calculate the storm momentum p_{storm} as the integral of the storm kinetic energy k over time,

$$p_{\text{storm}} = \int_t^{t+dt} k(t)\,dt = \int_t^{t+dt} \rho_a {U_{10}}^2(t)\,dt. \tag{4}$$

3 Storm impacts on mixed layer and sea ice properties

3.1 Case study

We begin by quantifying the immediate and seasonal impacts of one storm forced on August 15, for 4 days, with a magnitude of 15 m/s (referred hereafter as the 'storm run'). We compare results to the reference run.

In the reference run, the heat flux at the ocean surface remains positive until September 7 (Figure 2a), indicating that the surface layer is gaining heat from the atmosphere. After this date, the heat flux reverses sign and the surface layer begins to lose heat to the atmosphere. In the storm run, the wind forcing induces a decrease of the surface heat flux during the 4-day storm; between August 15 and 19, it is around 42 W.m^{-2}, 10 W.m^{-2} less than in the reference run (Figure 2a). After the storm, however, the heat flux becomes larger than in the reference run, by approximately 13 W.m^{-2}, meaning the ocean takes up more heat than in the reference run. This difference gets smaller over the course of the run. The heat flux continues to decrease and reverses sign on September 11, 4 days later than in the reference run.

When the ocean surface temperature reaches the freezing point temperature, ice can form (e.g., Leppäranta, 1993). In the reference run, ice formation occurs on October 5, while in the storm run, ice formation is delayed by 5 days (Figure 2b,c). The surface heat flux decreases immediately by one order of magnitude when ice forms in both runs (Figure 2a). Note that the oscillations in heat flux visible from October onwards are artefacts of the model discretization (see section 5.1). The sea ice concentration reaches 100% in a few days (Figure 2c), and the sea ice thickness reaches its maximum on June 6 for both runs. At this date, the surface heat flux becomes positive again, marking the end of the freezing period (Figure 2a). Sea ice is slightly thicker in the storm run on June 6 (+2 cm, i.e. +1%).

Associated with these changes at the ocean surface are changes in the mixed layer properties. The mixed layer is initially 13.5 m deep and remains relatively constant at the beginning of the reference run (Figure 3a,d). In the storm run, the storm forces a nearly instantaneous 10 m deepening of the mixed layer (Figure 3b,e). It then remains relatively constant. When ice forms, the mixed layer is still approximately 10 m thicker in the storm run than in the reference run. During the freezing period, the mixed layer continuously deepens. On June 6, the mixed layer depths in both runs are very similar (+1 m in the storm run).

The mixed layer temperature in the reference run increases between August 1 and September 1 (from -1.23°C to its maximum value of 0.83°C; Figure 3c), before decreasing to reach the freezing point temperature on the ice formation date (-1.43°C on October 5). The mixed layer remains close to the freezing point temperature during the rest of the freezing period. The drivers of the mixed layer temperature variations are further investigated in section 4.1. In the storm run, the mixed layer temperature is cooled by the storm from 0.25°C to 0.17°C. The maximum temperature occurs 6 days later than in the reference run and is 0.46°C colder. The salinity increases from 26.4 to 26.9 psu due to the vertical entrainment of saltier water from below the mixed layer during the storm. This yields a 0.5 psu difference between the two runs on the respective ice formation dates, meaning that ice forms at a slightly lower freezing point temperature in the storm run (-1.45°C on October 10, see section 4.1). During the freezing period, the mixed layer temperature and salinity of the storm run converge towards the values of the reference run.

To summarize, the August storm deepens, cools, and increases the salinity of the mixed layer, resulting in a lower freezing point temperature. The storm's impact on the mixed layer leads to a delay of ice formation. Sea ice then forms more rapidly to reach a slightly higher sea ice thickness maximum in June, although the freezing period is shorter.

3.2 1D ensemble

We now expand our analysis to the large variety of storms tested in our 1D ensemble, in order to quantify the impact on sea ice as a function of the storm properties. We begin by examining the freeze-up date and the value of the sea ice thickness maximum reached at the end of the freezing period. Almost all the runs present an ice formation date that is delayed compared to the reference run for which ice forms on October 5 (Figure 4). The largest delay is of two weeks for the run with the strongest August 1 storm. The sea ice thickness maxima vary between 2 m and 2.11 m around the reference run sea ice thickness maximum of 2.01 m (up to a 5% change). For different storms of the same momentum, an earlier storm results in a later ice formation date, and a later storm results in a higher maximum sea ice thickness. Increasing storm momentum results in a later ice formation date and higher maximum ice thickness. There is a significant correlation ($R^2 \geq 0.88$) between ice thickness and ice formation date, for storms occurring in August and September: the later ice forms, the thicker sea ice this yields.

4 Storm-induced delay in sea ice formation

4.1 Case study

In this section, we perform a mixed layer temperature budget in order to decipher the different processes at play during the storm and quantify their relative importance. The rate of change of the mixed layer temperature evolves as (Vialard & Delecluse, 1998):

$$\partial_t T_m = \underbrace{\frac{Q_{\text{net}}}{\rho_0 C_p h}}_{1} + \underbrace{\frac{K_z \partial_z T}{h}\bigg|_h}_{2} + \underbrace{\partial_t h \frac{T_h - T_m}{h}}_{3}, \tag{5}$$

with T_m the mean mixed layer temperature, Q_{net} the total surface heat flux into the mixed layer, C_p the specific heat of sea water equal to 3992 J.kg^{-1}.K^{-1}, K_z the vertical eddy diffusivity, T the temperature (which both vary with depth), $\partial_t h$ the entrainment velocity at the base of the mixed layer (equal to 0 m/s when the mixed layer depth is constant or when it shoals), and T_h the temperature at the base of the mixed layer. Note that because summer mixed layers are shallow in the Beaufort Sea ($\sim$ 10 m; Peralta-Ferriz & Woodgate, 2015), part of the solar/shortwave radiation penetrates deeper than the mixed layer and does not contribute to heating it. Therefore Q_{net} does not include this portion of the solar/shortwave radiation (Paulson & Simpson, 1977), and is equal to the total heat flux at the ocean surface Q_s (solar/shortwave radiation, non-solar/longwave radiation, latent and sensible heat fluxes), minus the penetrative part of Q_s below the mixed layer. Term 1 represents the change in mixed layer temperature due to the total surface heat flux into the mixed layer. Term 2 represents the change in mixed layer temperature due to the vertical turbulent flux at the base of the mixed layer. Term 3 represents the change in mixed layer temperature due to the heat flux resulting from vertical entrainment at the base of the mixed layer.

In the reference and storm runs, from the beginning of the run to the October freeze-up, the evolution of mixed layer temperature (Figure 5b) is primarily driven by the atmospheric forcing at the ocean surface (Figure 5c). The rate of change of mixed layer temperature (Figure 5a) decreases approximately linearly and goes from positive to negative, following the same trend as the effect of surface heat flux, with the same amplitude (Figure 5c). In the reference run, the processes at the base of the mixed layer (vertical entrainment and vertical diffusion; Figure 5e,g) play a minor role for the mixed layer temperature evolution. Vertical entrainment is equal to zero, and vertical diffusion is two to three orders of magnitude smaller than the effect of surface processes. During the storm, the mixed layer temperature decrease (Figure 5b) is mainly due to the processes at the base of the mixed layer that force a cooling (Figure 5e,g), due to the presence of colder waters below the mixed layer (Figure 3). The vertical entrainment and vertical diffusion contribute to a cooling of -0.3°C and -0.5°C, respectively, during the storm. After the storm, the rate of change of mixed layer temperature is slower in the storm run due a weaker effect of the surface heat flux on the mixed layer (Figure 5c).

To better explain the delay is sea ice formation in the storm run, we calculate the integrated mixed layer heat content for both runs following Davis et al. (2016):

$$H_C = \rho_0 C_p \int_0^h [T(z,t) - T_{\text{FP}}(z,t)]\, dz, \tag{6}$$

with T_{FP} the freezing point temperature.

As the storm deepens the mixed layer and lowers the freezing point (Figure 5d,f), it also contributes to an increase in the mixed layer heat content (Figure 5h), despite the reduction in mixed layer temperature (Figure 5b). The mixed layer heat content reaches

1.7×10^8 J.m^{-2} at its maximum on September 7, compared to 1.2×10^8 J.m^{-2} on September 1 in the reference run. This increase is to first order driven by the increase in mixed layer depth rather than the decrease in freezing point temperature. They respectively contribute to +130% and +2% of the increase in mixed layer heat content, while the cooling of the mixed layer contributes to -32%. Because of this increase of mixed layer heat content in the storm run, the effect of surface heat flux on the mixed layer is weaker (Figure 5c). Consequently, the mixed layer takes longer to lose its heat during the fall season. In addition, as a result of increased salinity in the mixed layer, the freezing point is lower in the storm run (Figure 3f). The mixed layer therefore reaches the freezing point temperature later (Figure 5b,d). This leads to a delay in the date of freeze-up. Note that the heat content does not reach exactly 0 J.m^{-2} here because the temperature is not exactly at the freezing point at lower levels in the mixed layer.

4.2 1D ensemble

We now calculate the integrated mixed layer heat content from the beginning of the run to the ice formation date, for all 245 runs, as follows:

$$H_{C_{\text{int}}} = \int_{t_0}^{t_{\text{freeze}}} H_C \, dt, \tag{7}$$

with t_0 the beginning of the run on August 1, and t_{freeze} the ice formation date in October, which varies between the runs. Runs with larger storm momentum are runs with larger integrated mixed layer heat content (as large as 1.6×10^{15} J.s.m^{-2}, which is 3.2 times more than in the reference run; Figure 6). This result is sensitive to storm date: runs with a storm occurring in August result in the largest integrated mixed layer heat contents. The sensitivity to storm momentum is attributed to the fact that stronger storms cause a greater deepening of the mixed layer, resulting in a larger increase in heat content. This effect outweighs the cooling effect of the storm. The sensitivity to storm date is because storms in August result in a longer exposure of the thickened mixed layer to surface heating, allowing for greater heat content increase before the change of sign of the surface heat flux.

5 Storm-induced ice growth

5.1 Case study

In this section, we focus on the freezing period, in order to understand why sea ice forms more rapidly in the storm run during this period, in response to a storm occurring during the open water period.

At the beginning of October, sea ice is thinner in the storm run than in the reference run (Figure 7a), due to the earlier ice formation in the reference run. By the end of November, the sea ice is thicker in the storm run and remains so, leading to an extra 2 cm of sea ice at the end of the freezing period (Figure 7a). We quantify the ice formation rate e_{ice} as

$$e_{\text{ice}} = \frac{h_{\max}}{t_{\text{melt}} - t_{\text{freeze}}}, \tag{8}$$

with $h_{\max}$ the sea ice thickness maximum at the end of the freezing period, and t_{melt} the ice melt date in June which corresponds to the date of sea ice thickness maximum. The ice formation rate is of 8.45 mm/day and 8.25 mm/day for the storm and reference runs, respectively. Concomitantly, the mixed layers in both runs deepen over the course of the

freezing period (Figure 7b), with a smaller deepening in the storm run (17 m compared to 25 m in the reference run).

For the mixed layer temperature budget of both runs, we only show the effect of vertical entrainment on the rate of change of mixed layer temperature as it is the largest contribution during the freezing period (Figure 7c). When the mixed layer deepens by a depth bin of 1 m (Figure 7b), the effect of vertical entrainment on the rate of change of mixed layer temperature increases during that time step (reaching values on the order of 1×10^{-6} °C/s), and becomes the dominant term of the budget (by one and two orders of magnitude; not shown). This causes the mixed layer to warm (peaks in Figure 7d), due to the presence of warmer waters below the mixed layer (Figure 3). When warm waters are entrained into the mixed layer and the surface temperature suddenly increases, this causes a deviation from the surface freezing point temperature (Figure 7d). The surface temperature then converges back to the freezing point as the surface heat flux is negative (Figure 2a), which allows ice to grow again. When the mixed layer depth does not vary, the effect of the surface heat flux is the dominant term (not shown).

Given that the mixed layer depth changes less over the course of the freezing period in the storm run than the reference run (Figure 7b), the cumulative effect of the vertical entrainment is smaller (by a factor of 2; Figure 7c). The storm run presents fewer deviations from the freezing point, allowing ice to form more rapidly (0.20 mm/day difference), explaining why sea ice is thicker at the end of the freezing period in this run. Note that the steps and peaks in the time series of Figure 7 are a consequence of the model discretization.

5.2 1D ensemble

We then investigate how this result is sensitive to the properties of the storm. In all 245 runs, we calculate the total energy into the mixed layer from vertical entrainment E_{VE} as follows:

$$E_{\mathrm{VE}} = \rho_0 C_p \int_{t_{\mathrm{freeze}}}^{t_{\mathrm{melt}}} \partial_t h \, (T_h - T_m) \, dt. \tag{9}$$

Sea ice thickness maximum is anti-correlated with the cumulative energy into the mixed layer due to the vertical entrainment ($\mathrm{R}^2 = 0.84$; Figure 8a). It is also correlated with the mixed layer depth on ice formation date ($\mathrm{R}^2 = 0.88$; Figure 8b), which in turn depends on the momentum of the storm. These correlations mean that the stronger the storm is, the thicker mixed layer it sets, the less energy is entrained in the mixed layer after ice formation begins, and the thicker the sea ice can grow. Note that these correlations seem independent from the date of storm and only significantly dependent on the storm momentum as it sets the mixed layer depth to first order. The heat of fusion is ~ 330 kJ/kg, which means that an input of 3.3 MJ of energy into the mixed layer would prevent 1 cm of ice formation. We integrate each term of equation 5 between t_{freeze} and t_{melt} and estimate that one third of the energy that is entrained into the mixed layer affects the formation of the ice and two thirds are released to the atmosphere.

6 Mechanical and buoyancy forcing during the storm

In this section, we quantify the relative contributions of the surface forcing in driving the changes in mixed layer depth during and after the storms. The latter are: buoyancy (heat and freshwater fluxes at the ocean surface), wind, and waves (wave breaking, Stokes drift, and Langmuir turbulence). We use the same framework as Belcher et al. (2012) to calculate the scaled production terms of the TKE equation (equation 2). In our 1D model, the wave-forced production term is proportional to the wind-forced pro-

duction term of TKE by a factor of approximately 12, due to the model parametrization (see section 2.1). We therefore combine these two effects into one scaled term referred to as the 'mechanical-forced production of TKE'. The scaled production terms of TKE are as follows:

$$B_s = B_{\mathrm{HF}} + B_{\mathrm{FWF}} = -g\alpha \frac{Q_s}{\rho_s C_p} + g\beta F_s^w S_s, \tag{10}$$

$$W_d + W_s = \frac{u_*^3}{h} + \frac{u_*^2 u_{\mathrm{SD}_0}}{h}, \tag{11}$$

where the buoyancy-forced production term B_s is defined as the sum of the heat B_{HF} and freshwater B_{FWF} fluxes contributions to the buoyancy flux, with α the thermal expansion coefficient, ρ_s the surface density, β the haline contraction coefficient, F_s^w the freshwater flux at the ocean surface and S_s the surface salinity. The wind and wave-forced production terms are W_d and W_s, respectively, and their sum is the mechanical-forced production term of TKE. The friction velocity in water is defined as: $u_* = \sqrt{|\boldsymbol{\tau}|/\rho_s}$. From this framework, we compute the ratio of buoyancy to mechanical-forced production of TKE.

6.1 Case study

We first examine the open water period. In the reference run, B_s is negative from August 1 to September 7, and positive after September 7 (Figure 9c; note that a negative buoyancy-forced production of TKE is a destruction of TKE). This term is to first order driven by the heat flux contribution during the open water period (Figure 9a). As discussed in section 3.1, the surface layer gains heat and becomes more buoyant until the end of summer. When the surface heat flux changes sign in September (Figure 2a), the ocean releases heat, the surface cools and loses buoyancy and the mixed layer deepens. During the storm, the buoyancy-forced destruction of TKE is reduced (from $B_s = -5.5\times 10^{-9}$ to $B_s = -1.2\times10^{-9}$ W/kg; Figure 9c) as the storm drives an increase of the heat and freshwater flux contributions to B_s (due to increased latent and sensible fluxes, and increased evaporation; Figure 9a). After the storm, B_s is larger than in the reference run due to the decrease of mixed layer temperature (Figure 5b) which increases the sensible heat flux at the surface. The change of sign of B_s in the storm run happens on September 12 with a 4-day delay compared to the reference run. B_s eventually becomes larger than in the reference run on September 22, for the same reasons as right after the storm.

The mechanical-forced production of TKE remains relatively constant in the reference run (Figure 9e), consistent with the constant wind forcing. In the storm run, it experiences a significant increase during the storm (from 1.3×10^{-7} to 8.4×10^{-6} W/kg), as the latter generates TKE within the mixed layer. After the storm, it decreases and stabilizes at lower values than in the reference run. Despite the mechanical forcing remaining unchanged from before the storm, it acts over a thicker mixed layer after the storm. This results in a weaker shear, leading to reduced TKE generation.

The mechanical-forced production of TKE is always greater than the buoyancy-forced production or destruction of TKE (Figure 9g). It therefore drives, at first order, the changes in mixed layer depth during the open water period. This is especially true during the storm when the mechanical-forced production of TKE is 3 orders of magnitude larger than the buoyancy-forced production. After the storm, the ratio is larger than in the reference run because the buoyancy-forced production and the mechanical-forced production terms are lower and larger respectively, as discussed above.

During the freezing period, the wave forcing is zero as soon as the sea ice concentration reaches 25% (section 2.1). We therefore only present results for the buoyancy and

wind-forced productions of TKE (Figure 9d,f). In contrast to the open water period, the buoyancy-forced production of TKE (Figure 9d) is to first order driven by the freshwater flux contribution (the heat flux contribution is two orders of magnitude smaller and is therefore barely visible on Figure 9b). This is due to brine rejection which decreases the buoyancy at the surface and generates convective mixing. The freshwater flux is stronger in the storm run, especially in October when ice is forming more rapidly (section 5.1). The wind-forced production term of TKE is lower in the storm run (Figure 9f) similarly as during the open water period, due to the thicker mixed layer generated by the storm.

The buoyancy-forced production is larger by 3 orders of magnitude than the wind-forced production of TKE (Figure 9h), due to a strong reduction of the surface stress in the presence of ice. In contrast to the open water period, it is therefore the buoyancy forcing essentially driving the changes in mixed layer depth during the freezing period. The ratio is larger in the storm run because the wind-forced production term of TKE is lower than in the reference run due to the difference in mixed layer thicknesses.

6.2 1D ensemble

We integrated the TKE production terms in time, during the open water period, and the freezing period (not shown). In all runs, similarly to the storm run, the net effect of buoyancy forcing on TKE production during the open water period was less than approximately 1% of that of mechanical forcing. Conversely, during the freezing period, buoyancy forcing typically contributed between 50 and 700 times more to TKE production than wind-forcing.

7 Sensitivity to different initial profiles representative of future conditions for the Canadian Basin

Observational studies have documented a stronger Canadian Basin (Rosenblum et al., 2022) and pan-Arctic stratification in summer (Peralta-Ferriz & Woodgate, 2015). With stronger sea ice melt, especially in summer, and increased freshwater input from river runoff, along with a projected increase by approximately 30% of precipitations minus evaporation by 2050 (e.g., Notz & Community, 2020; Haine et al., 2015), the Canadian Basin is likely shifting towards a more stratified ocean, at least during summer. In this section, we explore if the impact of a given storm is sensitive to the stratification on which it applies. To that end, we conduct the same ensemble of runs described in section 2.2, but with initial conditions that are representative of a more stratified Canadian Basin. The initial profiles are the mean of four CTD casts located within 1° of latitude and 3.3° of longitude of the BGEPA mooring, from August 2007 (Figure 10). We choose this date because of the presence of a very shallow mixed layer of 1 m, and a strong surface stratification, likely originating from the increased sea ice melt that occurred in 2007 (Stroeve et al., 2008). For the years with CTD data near the mooring in August (2005, 2006, 2007, 2012, 2013 and 2021), only 2007 had such a strong surface stratification. For this initial condition, the NSTM is 10 m shallower and 1°C warmer compared to the initial condition used in the 1D ensemble. The surface temperature is also 0.8°C warmer, meaning that the top 30 m of the ocean contain more heat in this case.

7.1 NSS case study

In the reference run of this near-surface stratification (NSS) ensemble of runs (referred to as 'NSS reference run'), the high stratification is not maintained very long (Figure 11a,d): 9 hours after the beginning of the run, the mixed layer increases by 1 m. It then deepens gradually and reaches 6.5 m on September 29 (ice formation date), which is 6 m shallower than the mixed layer in the previous reference run (12.5 m on ice formation date).

In the example storm run of the NSS ensemble (referred to as 'NSS storm run'), the mixed layer deepens rapidly on August 15 from 5.5 to 19.5 m (Figure 11b,e). The relative deepening induced by the storm in this run is larger here than in the storm run studied in sections 3 to 6 (14 m deepening compared to 11 m). Nevertheless, the mixed layer depth is still shallower after the storm in the NSS storm run. This is also the case on the ice formation date (15.5 m compared to 20.5 m in the previous storm run). Sea ice forms on September 29 in the NSS reference run, while in the NSS storm run, ice formation is delayed by 9 days (Figure 11), which is twice the delay between the previous reference and storm runs. With a different initial stratification, the delay in sea ice formation caused by the same storm is therefore significantly longer.

7.2 NSS ensemble

In this section we present results for a smaller number of runs for the NSS ensemble (196 compared to 245 runs in the 1D ensemble) as we do not force storms on October 1 because ice has already formed at this date in the NSS reference run. We find that this is because mixed layers in the NSS ensemble experience a greater cooling in fall (e.g., Figure 11c) than in the 1D ensemble, as they are thinner during the open water period. For same Q_{net}, if h is smaller, the change in mixed layer temperature due to the total surface heat flux is greater (term 1 in equation 5). This leads to earlier ice formation date in the NSS reference run and in runs with a low momentum storm.

When generalizing to all runs, we find that the storm impacts studied in the 1D ensemble are similar for the NSS ensemble, but amplified. The ice formation dates are delayed for the runs with a storm, and the stronger the storm is, the longer the delay (Figure 12a). The maximum delay is of 20 days, which is 5 days more than in the 1D ensemble. The largest integrated heat content (1.6×10^{15} J.s.m^{-2}; Figure 12b) is 6.2 times greater than the integrated heat content in the NSS reference run, which is twice as much increase than found in the 1D ensemble (although the storm-induced cooling for this NSS run is even larger: -1°C compared to -0.2 °C for the corresponding storm run in the 1D ensemble). This is due to the larger differences in mixed layer thicknesses after the storm, between the NSS runs with a storm and the NSS reference run. The mixed layers of these runs therefore experience a longer decrease of mixed layer heat content. The freezing point temperature is consequently reached with a longer delay in the NSS ensemble than in the 1D ensemble. Note that although the initial temperature profile for the NSS ensemble is warmer in the top 30 m (Figure 10), the integrated mixed layer heat content in NSS reference run (Figure 12b) is 0.2×10^{15} J.s.m^{-2} smaller than in the previous reference run (Figure 6), due to a thinner mixed layer throughout the run. The temperature of the initial profile therefore does not play an important role here, it is rather the thickness of the mixed layer that sets the mixed layer heat content.

In the NSS ensemble, we again find that the storms allow for an increase of the sea ice thickness maxima compared to the NSS reference run (values range between 1.99 and 2.13 m compared to 1.99 m in the NSS reference run), and the later the storm happens, the stronger this effect is (Figure 12a). The maximum difference is of 14 cm (4 cm more than in the 1D ensemble). This is again due to the deeper mixed layers after the storm compared to the NSS reference run in the NSS ensemble: they prevent warm water entrainment and favour sea ice growth (as studied in section 5). Correlation coefficients between the sea ice thickness maxima and the ice formation dates are again significant ($R^2 \geq 0.91$).

Results for the NSS ensemble suggest that in the case of strongly stratified water column, if a storm passes, the consequences on the date of sea ice formation may be even more important than in the case of a water column with a deeper mixed layer. For this type of stratification, storms can yield a faster sea ice growth compared to the case with a deeper mixed layer.

8 Conclusion

In this paper, we used a 1D ice-ocean coupled model and forced individual storms characterized by varying properties (storm date, intensity, and duration), to investigate how these events impact the seasonal dynamics. We showed that the date of freeze-up in the fall is delayed when a storm occurs during the open water period, compared to a reference run with no storm. The delay can be up to 20 days depending on the initial stratification and the storm properties. This result is significant compared to the interannual variability in sea ice formation date, which was reported to be on the order of days at the center of the Beaufort Sea between 2003 and 2018 (Lin et al., 2022). This delay is caused by a storm-induced increase of the mixed layer heat content (although the mixed layer cools), primarily due to the deepening of the mixed layer by the mechanical forcing of the storm. The delay in sea ice formation is greater when storms are stronger as they force an important deepening of the mixed layer, and when storms occur earlier in summer. The deep mixed layers generated by early-summer storms are heated by the atmospheric forcing until the surface heat flux changes sign at the end of summer. This allows for higher heat contents than the runs with storms happening later in summer.

After the storm, the mixed layer remains deep, preventing warm water entrainment into the mixed layer during the freezing period. Ice therefore grows faster: it can produce up to 14 cm extra sea ice by the end of the freezing period for a 47.5 m mixed layer run (at freeze-up date) compared to a 6.5 m mixed layer run. As the momentum of the storm drives a mixed layer thickness anomaly before the beginning of the freezing period, stronger momentum storms allow for longer delays in sea ice formation and stronger ice growth. Over the period 2003-2011, the interannual variations of sea ice thickness maxima at the BGEPA mooring are up to 1 m (Krishfield et al., 2014). Our results suggest that one storm can contribute up to approximately 10% of the interannual variability, which highlights the potential important effect that a short term event can have on the seasonal cycle of sea ice.

Short-term storm-generated changes in the mixed layer properties have been previously observed in the Beaufort Sea by Smith et al. (2018). Their study takes place later than ours (in mid-October), when the stratification presents warm waters below a cold mixed layer and ice has already formed. They measured a release of heat of 10 $MJ.m^{-2}$ and a 5 m mixed layer deepening due to a 3-day wind and wave event (up to 20 m/s and greater than 4 m, respectively). This caused the melt of the pancake ice present prior the event, ice then re-formed a few days later. For an October 1 storm of comparable duration and magnitude from our study, our model suggests that the mixed layer is deepened by 20 m, and the freeze-up delay is of 4 days. This leads to a formation of an extra 6 cm of ice at the end of the freezing period. Albeit acting on a different stratification, our results suggest that the event described by Smith et al. (2018) could have resulted in a significant sea ice thickening at the end of the freezing season.

Although we are confident that the dominant dynamical balance is captured by the 1D model we used, some limitations remain which merit further exploration. In this configuration we use a parametrization of the waves as a function of the wind speed which is unable to capture the effects of varying fetch. Advective processes for the sea ice and the ocean are not represented in a 1D configuration, and our results may change when adding them. For example, zones of increased mixed layer heat content or anomalies in sea ice thickness caused by storms could be advected and potentially dissipated by horizontal movement in the months that follow. Upper ocean mixing generated by small-scale frontal structures, filaments and eddies (e.g., Brenner et al., 2020) are also not captured by the 1D configuration. Storms could have a spatially variable impact on the mixed layer and the sea ice, depending on the 3D imprint of the event (Clancy et al., 2022). Therefore, using a 3D configuration and a 2D representation of a storm (shape and track) to investigate its seasonal effects on the ocean and sea ice, would allow testing the vari-

ability of these results in a more realistic set up. The focus of our work was to understand the effects of forcing by wind events. However, storms also have impacts on other atmospheric variables such as heat flux and precipitation. For example, Finocchio and Doyle (2021) showed that changes in cloud cover and shortwave flux associated with summer Arctic cyclones could affect sea ice locally. The atmospheric forcing could therefore be adapted to more realistically simulate Arctic cyclones. Finally, this study could also be expanded by testing the sensitivity of the results when multiple storms are forced during the open water period.

The significant wave height and its extremes in the Arctic Ocean are expected to increase in the future, driven by the loss of sea ice (Khon et al., 2014; Casas-Prat et al., 2018). Studies project increasing trends of wind speeds over the 21st century (Vavrus & Alkama, 2021), cyclone frequency could increase in summer (Day et al., 2018). In the context of declining sea ice, the surface mechanical forcing will likely increase in magnitude and extent, potentially changing the ocean stratification during the open water period. We therefore suggest that the processes presented in this study may become of greater importance in the future, and drive changes in seasonal sea ice evolution.

Open Research Section

The NEMO1D configuration is based on the version 4.2 of the NEMO code, that can be downloaded at: https://forge.nemo-ocean.eu/nemo/nemo/-/releases/4.2.1. The sea ice concentration data is from EUMETSAT Ocean and Sea Ice Satellite Application Facility (OSI SAF) and can be downloaded at: https://osi-saf.eumetsat.int/products/sea-ice-products. The BGEPA mooring data and CTD cast data are made available at: https://www2.whoi.edu/site/beaufortgyre/data/mooring-data/mooring-data-description/. The Drakkar Forcing Set 5.2 data can be downloaded at: https://www.drakkar-ocean.eu/forcing-the-ocean.

Acknowledgments

This project has received funding from the European Research Council (ERC) under the European Union's Horizon 2020 research and innovation programme (grant agreement No 805186). Support for a partial Ph.D. studentship was provided by the ISblue project, Interdisciplinary graduate school for the blue planet (ANR-17-EURE-0015). We thank Claude Talandier who has largely contributed to the set up of the NEMO1D configuration.

References

Asplin, M. G., Galley, R., Barber, D. G., & Prinsenberg, S. (2012). Fracture of summer perennial sea ice by ocean swell as a result of Arctic storms. *Journal of Geophysical Research: Oceans*, *117*(C6). doi: https://doi.org/10.1029/2011JC007221

Asplin, M. G., Scharien, R., Else, B., Howell, S., Barber, D. G., Papakyriakou, T., & Prinsenberg, S. (2014). Implications of fractured Arctic perennial ice cover on thermodynamic and dynamic sea ice processes. *Journal of Geophysical Research: Oceans*, *119*(4), 2327–2343. doi: https://doi.org/10.1002/2013JC009557

Axell, L. B. (2002). Wind-driven internal waves and Langmuir circulations in a numerical ocean model of the southern Baltic Sea. *Journal of Geophysical Research*, *107*(C11), 3204. doi: https://doi.org/10.1029/2001JC000922

Belcher, S. E., Grant, A. L. M., Hanley, K. E., Fox-Kemper, B., Van Roekel, L., Sullivan, P. P., ... Polton, J. A. (2012). A global perspective on Langmuir turbulence in the ocean surface boundary layer. *Geophysical Research Letters*,

39(18). doi: https://doi.org/10.1029/2012GL052932

Blanke, B., & Delecluse, P. (1993). Variability of the Tropical Atlantic Ocean Simulated by a General Circulation Model with Two Different Mixed-Layer Physics. *Journal of Physical Oceanography*, *23*(7), 1363–1388. doi: https://doi.org/10.1175/1520-0485(1993)023⟨1363:VOTTAO⟩2.0.CO;2

Boutin, G., Lique, C., Ardhuin, F., Rousset, C., Talandier, C., Accensi, M., & Girard-Ardhuin, F. (2020). Towards a coupled model to investigate wave–sea ice interactions in the Arctic marginal ice zone. *The Cryosphere*, *14*(2), 709–735. doi: https://doi.org/10.5194/tc-14-709-2020

Brenner, S., Rainville, L., Thomson, J., & Lee, C. (2020). The evolution of a shallow front in the Arctic marginal ice zone. *Elementa: Science of the Anthropocene*, *8*, 17. doi: https://doi.org/10.1525/elementa.413

Casas-Prat, M., Wang, X., & Swart, N. (2018). CMIP5-based global wave climate projections including the entire Arctic Ocean. *Ocean Modelling*, *123*, 66-85. doi: https://doi.org/10.1016/j.ocemod.2017.12.003

Clancy, R., Bitz, C. M., Blanchard-Wrigglesworth, E., McGraw, M. C., & Cavallo, S. M. (2022). A cyclone-centered perspective on the drivers of asymmetric patterns in the atmosphere and sea ice during arctic cyclones. *Journal of Climate*, *35*(1), 73 - 89. doi: https://doi.org/10.1175/JCLI-D-21-0093.1

Collins, C. O., Rogers, W. E., Marchenko, A., & Babanin, A. V. (2015). In situ measurements of an energetic wave event in the Arctic marginal ice zone. *Geophysical Research Letters*, *42*(6), 1863–1870. doi: https://doi.org/10.1002/2015GL063063

Couvelard, X., Lemarié, F., Samson, G., Redelsperger, J.-L., Ardhuin, F., Benshila, R., & Madec, G. (2020). Development of a two-way-coupled ocean–wave model: assessment on a global NEMO(v3.6)–WW3(v6.02) coupled configuration. *Geoscientific Model Development*, *13*(7), 3067–3090. doi: https://doi.org/10.5194/gmd-13-3067-2020

Craig, P. D., & Banner, M. L. (1994). Modeling wave-enhanced turbulence in the ocean surface layer. *Journal of Physical Oceanography*, *24*(12), 2546 - 2559. doi: https://doi.org/10.1175/1520-0485(1994)024⟨2546:MWETIT⟩2.0.CO;2

Davis, P. E. D., Lique, C., Johnson, H. L., & Guthrie, J. D. (2016). Competing Effects of Elevated Vertical Mixing and Increased Freshwater Input on the Stratification and Sea Ice Cover in a Changing Arctic Ocean. *Journal of Physical Oceanography*, *46*(5), 1531–1553. doi: https://doi.org/10.1175/JPO-D-15-0174.1

Day, J. J., Holland, M. M., & Hodges, K. I. (2018). Seasonal differences in the response of Arctic cyclones to climate change in CESM1. *Climate dynamics*, *50*(9), 3885–3903. doi: https://doi.org/10.1007/s00382-017-3767-x

de Boyer Montégut, C., Madec, G., Fischer, A. S., Lazar, A., & Iudicone, D. (2004). Mixed layer depth over the global ocean: An examination of profile data and a profile-based climatology. *Journal of Geophysical Research: Oceans*, *109*(C12). doi: https://doi.org/10.1029/2004JC002378

Dohan, K., & Davis, R. E. (2011). Mixing in the transition layer during two storm events. *Journal of Physical Oceanography*, *41*(1), 42 - 66. doi: https://doi.org/10.1175/2010JPO4253.1

Dussin, R., Barnier, B., Brodeau, L., & Molines, J.-M. (2016). *The making of the Drakkar Forcing set DFS5.* Zenodo. doi: https://doi.org/10.5281/zenodo.1209243

D'Alessio, S. J. D., Abdella, K., & McFarlane, N. A. (1998). A new second-order turbulence closure scheme for modeling the oceanic mixed layer. *Journal of Physical Oceanography*, *28*(8), 1624 - 1641. doi: https://doi.org/10.1175/1520-0485(1998)028⟨1624:ANSOTC⟩2.0.CO;2

Finocchio, P. M., & Doyle, J. D. (2021). Summer Cyclones and Their Association With Short-Term Sea Ice Variability in the Pacific Sector of the Arctic. *Fron-*

tiers in Earth Science, *9*. doi: https://doi.org/10.3389/feart.2021.738497

Fofonoff, N., & Millard Jr, R. (1983). Algorithms for Computation of Fundamental Properties of Seawater. Endorsed by Unesco/SCOR/ICES/IAPSO Joint Panel on Oceanographic Tables and Standards and SCOR Working Group 51. *Unesco Technical Papers in Marine Science*, *44*.

G. Madec and the NEMO System Team. (2019). *NEMO ocean engine* (Tech. Rep. No. 27). Institut Pierre-Simon Laplace (IPSL). doi: https://doi.org/10.5281/zenodo.1464816

Haine, T. W., Curry, B., Gerdes, R., Hansen, E., Karcher, M., Lee, C., ... Woodgate, R. (2015). Arctic freshwater export: Status, mechanisms, and prospects. *Global and Planetary Change*, *125*, 13-35. doi: https://doi.org/10.1016/j.gloplacha.2014.11.013

Jackson, J. M., Carmack, E. C., McLaughlin, F. A., Allen, S. E., & Ingram, R. G. (2010). Identification, characterization, and change of the near-surface temperature maximum in the Canada Basin, 1993–2008. *Journal of Geophysical Research: Oceans*, *115*(C5). doi: https://doi.org/10.1029/2009JC005265

Khon, V. C., Mokhov, I. I., Pogarskiy, F. A., Babanin, A., Dethloff, K., Rinke, A., & Matthes, H. (2014). Wave heights in the 21st century Arctic Ocean simulated with a regional climate model. *Geophysical Research Letters*, *41*(8), 2956-2961. doi: https://doi.org/10.1002/2014GL059847

Krishfield, R. A., Proshutinsky, A., Tateyama, K., Williams, W. J., Carmack, E. C., McLaughlin, F. A., & Timmermans, M.-L. (2014). Deterioration of perennial sea ice in the beaufort gyre from 2003 to 2012 and its impact on the oceanic freshwater cycle. *Journal of Geophysical Research: Oceans*, *119*(2), 1271-1305. doi: https://doi.org/10.1002/2013JC008999

Kwok, R. (2018). Arctic sea ice thickness, volume, and multiyear ice coverage: losses and coupled variability (1958–2018). *Environmental Research Letters*, *13*(10), 105005. doi: https://doi.org/10.1088/1748-9326/aae3ec

Lemke, P., & Manley, T. O. (1984). The seasonal variation of the mixed layer and the pycnocline under polar sea ice. *Journal of Geophysical Research: Oceans*, *89*(C4), 6494-6504. doi: https://doi.org/10.1029/JC089iC04p06494

Leppäranta, M. (1993). A review of analytical models of sea-ice growth. *Atmosphere-Ocean*, *31*(1), 123-138. doi: https://doi.org/10.1080/07055900.1993.9649465

Li, M., & Garrett, C. (1993). Cell merging and the jet/downwelling ratio in Langmuir circulation. *Journal of Marine Research*, *51*(4), 737–769.

Lin, L., Lei, R., Hoppmann, M., Perovich, D. K., & He, H. (2022). Changes in the annual sea ice freeze–thaw cycle in the Arctic Ocean from 2001 to 2018. *The Cryosphere*, *16*(12), 4779–4796. doi: https://doi.org/10.5194/tc-16-4779-2022

Lindsay, R., Wensnahan, M., Schweiger, A., & Zhang, J. (2014). Evaluation of seven different atmospheric reanalysis products in the Arctic. *Journal of Climate*, *27*(7), 2588 - 2606. doi: https://doi.org/10.1175/JCLI-D-13-00014.1

Long, Z., & Perrie, W. (2012). Air-sea interactions during an Arctic storm. *Journal of Geophysical Research: Atmospheres*, *117*(D15). doi: https://doi.org/10.1029/2011JD016985

Mellor, G., & Blumberg, A. (2004). Wave breaking and ocean surface layer thermal response. *Journal of Physical Oceanography*, *34*(3), 693 - 698. doi: https://doi.org/10.1175/2517.1

NEMO Sea Ice Working Group. (2019). *Sea Ice modelling Integrated Initiative (SI^3) – The NEMO sea ice engine* (Tech. Rep. No. 31). Institut Pierre-Simon Laplace (IPSL). doi: https://doi.org/10.5281/zenodo.1471689

Notz, D., & Community, S. (2020). Arctic Sea Ice in CMIP6. *Geophysical Research Letters*, *47*(10). doi: https://doi.org/10.1029/2019GL086749

Paulson, C. A., & Simpson, J. J. (1977). Irradiance measurements in the upper ocean. *Journal of Physical Oceanography*, *7*(6), 952 - 956. doi: https://doi

.org/10.1175/1520-0485(1977)007⟨0952:IMITUO⟩2.0.CO;2

Peralta-Ferriz, C., & Woodgate, R. A. (2015). Seasonal and interannual variability of pan-Arctic surface mixed layer properties from 1979 to 2012 from hydrographic data, and the dominance of stratification for multiyear mixed layer depth shoaling. *Progress in Oceanography*, *134*, 19-53. doi: https://doi.org/10.1016/j.pocean.2014.12.005

Proshutinsky, A., Krishfield, R., Timmermans, M.-L., Toole, J., Carmack, E., McLaughlin, F., ... Shimada, K. (2009). Beaufort Gyre freshwater reservoir: State and variability from observations. *Journal of Geophysical Research: Oceans*, *114*(C1). doi: https://doi.org/10.1029/2008JC005104

Reffray, G., Bourdalle-Badie, R., & Calone, C. (2015). Modelling turbulent vertical mixing sensitivity using a 1-D version of NEMO. *Geoscientific Model Development*, *8*(1), 69–86. doi: https://doi.org/10.5194/gmd-8-69-2015

Regan, H. C., Lique, C., & Armitage, T. W. K. (2019). The Beaufort Gyre Extent, Shape, and Location Between 2003 and 2014 From Satellite Observations. *Journal of Geophysical Research: Oceans*, *124*(2), 844-862. doi: https://doi.org/10.1029/2018JC014379

Rosenblum, E., Stroeve, J., Gille, S. T., Lique, C., Fajber, R., Tremblay, L. B., ... Lukovich, J. V. (2022). Freshwater input and vertical mixing in the Canada Basin's seasonal halocline: 1975 versus 2006–12. *Journal of Physical Oceanography*, *52*(7), 1383 - 1396. doi: https://doi.org/10.1175/JPO-D-21-0116.1

Screen, J. A., Simmonds, I., & Keay, K. (2011). Dramatic interannual changes of perennial Arctic sea ice linked to abnormal summer storm activity. *Journal of Geophysical Research: Atmospheres*, *116*(D15). doi: https://doi.org/10.1029/2011JD015847

Smith, M., Stammerjohn, S., Persson, O., Rainville, L., Liu, G., Perrie, W., ... Thomson, J. (2018). Episodic Reversal of Autumn Ice Advance Caused by Release of Ocean Heat in the Beaufort Sea. *Journal of Geophysical Research: Oceans*, *123*(5), 3164-3185. doi: https://doi.org/10.1002/2018JC013764

Stopa, J. E., Ardhuin, F., & Girard-Ardhuin, F. (2016). Wave climate in the Arctic 1992–2014: seasonality and trends. *The Cryosphere*, *10*(4), 1605–1629. doi: https://doi.org/10.5194/tc-10-1605-2016

Stroeve, J., Serreze, M., Drobot, S., Gearheard, S., Holland, M., Maslanik, J., ... Scambos, T. (2008). Arctic sea ice extent plummets in 2007. *Eos, Transactions American Geophysical Union*, *89*(2), 13-14. doi: https://doi.org/10.1029/2008EO020001

Stroeve, J., Serreze, M. C., Holland, M. M., Kay, J. E., Malanik, J., & Barrett, A. P. (2012). The Arctic's rapidly shrinking sea ice cover: a research synthesis. *Climatic change*, *110*(3), 1005–1027. doi: https://doi.org/10.1007/s10584-011-0101-1

Thomson, J., & Rogers, W. E. (2014). Swell and sea in the emerging Arctic Ocean. *Geophysical Research Letters*, *41*(9), 3136–3140. doi: https://doi.org/10.1002/2014GL059983

Thomson, J., Smith, M., Drushka, K., & Lee, C. (2022). Air-Ice-Ocean Interactions and the Delay of Autumn Freeze-Up in the Western Arctic Ocean. *Oceanography*. doi: https://doi.org/10.5670/oceanog.2022.124

Toole, J. M., Timmermans, M.-L., Perovich, D. K., Krishfield, R. A., Proshutinsky, A., & Richter-Menge, J. A. (2010). Influences of the ocean surface mixed layer and thermohaline stratification on Arctic Sea ice in the central Canada Basin. *Journal of Geophysical Research: Oceans*, *115*(C10). doi: https://doi.org/10.1029/2009JC005660

Vavrus, S. J., & Alkama, R. (2021). Future trends of Arctic surface wind speeds and their relationship with sea ice in CMIP5 climate model simulations. *Climate Dynamics*, 1–16. doi: https://doi.org/10.1007/s00382-021-06071-6

Vialard, J., & Delecluse, P. (1998). An OGCM Study for the TOGA Decade. Part

I: Role of Salinity in the Physics of the Western Pacific Fresh Pool. *Journal of Physical Oceanography*, *28*(6), 1071–1088. doi: https://doi.org/10.1175/1520-0485(1998)028⟨1071:AOSFTT⟩2.0.CO;2

Wadhams, P., Squire, V. A., Goodman, D. J., Cowan, A. M., & Moore, S. C. (1988). The attenuation rates of ocean waves in the marginal ice zone. *Journal of Geophysical Research: Oceans*, *93*(C6), 6799-6818. doi: https://doi.org/10.1029/JC093iC06p06799

Figure 1. (a) Position of the Beaufort Gyre Exploration Project mooring A (BGEPA) in the Beaufort Sea (red dot). The colored lines represent the mean sea ice edges (defined as the 15% sea ice concentration contour) for September 2007, 2012 and 2014 (yellow, blue and magenta lines respectively), obtained from the EUMETSAT Ocean and Sea Ice Satellite Application Facility (OSI SAF). (b) Initial temperature and salinity profiles (respectively red, bottom x-axis and blue, top x-axis) which are the mean of the 4 temperature and salinity CTD casts plotted in thin red and blue, respectively. (c) Zoom on the top 80 m of the profiles shown in (b). (d) Climatological seasonal cycle of the atmospheric forcing: 2-m air temperature and humidity (blue and green respectively), downward shortwave and downward longwave radiations at the sea surface (purple and orange respectively and black y-axis on the right). (e) Wind forcing used for the reference run (red dashed line) and for the storm run presented in sections 3 to 6 (cyan line).

Figure 2. Time series of (a) the heat flux at the ocean surface, (b) sea ice thickness, and (c) sea ice concentration, for the reference and storm runs (red and cyan respectively). A positive heat flux is downward. The orange shading indicates the period of the storm. The vertical red and cyan lines represent the ice formation dates in the reference and storm runs respectively.

Figure 3. Time-depth diagrams of the temperature and salinity for (a, d) the reference run and (b, e) the storm run. The mixed layer depths are indicated in grey. The vertical orange lines indicate the beginning of the storm. The vertical dashed lines represent the ice formation dates in the reference and storm runs (red and cyan respectively). The vertical dotted lines represent the ice melt dates in the reference and storm runs (red and cyan respectively). (c, f) Time series of the mixed layer temperature and salinity for the reference and storm runs (red and cyan respectively). The orange shadings indicate the period of the storm, the vertical lines are the same as in the previous panels.

Figure 4. Sea ice thickness maximum plotted as a function of the ice formation date in each run of the 1D ensemble. The color of each dot indicates the date of the storm and its size its total momentum. The results for the reference and storm runs are shown with the red and black crosses, respectively.

Figure 5. Time series for the open water period of the mixed layer temperature budget with (a) the rate of change of mixed layer temperature, (c) the effect of surface heat flux, (e) the effect of vertical entrainment from below the mixed layer, and (g) the effect of vertical turbulent diffusive flux. Panels (a, c, e and g) also present the cumulative effect of the terms (colored shading and grey y-axis). Time series of (b) the mixed layer temperature, (d) the mixed layer freezing point temperature, (f) the mixed layer depth, and (h) the mixed layer heat content. The reference and storm runs are plotted in red and cyan respectively. The orange shadings indicate the period of the storm. The vertical red and cyan lines represent the ice formation dates in the reference and storm runs respectively.

Figure 6. Integrated mixed layer heat content during the open water period plotted as a function of storm momentum in each run of the 1D ensemble. The color of each dot indicates the date of the storm. The results for the reference and storm runs are shown with the red and black crosses, respectively.

Figure 7. Time series for the freezing period of: (a) the sea ice thickness difference between the reference and storm runs, (b) the mixed layer depth, (c) the effect of vertical entrainment heat flux (dominant term of the mixed layer temperature budget), along with its cumulative effect (colored shading and grey y-axis), and (d) the surface temperature and surface freezing point temperature (estimated from the surface salinity). The time series for the reference and storm runs are plotted in red and cyan respectively. Vertical red and cyan lines represent the ice formation dates in the reference and storm runs respectively.

Figure 8. Sea ice thickness maximum plotted as a function of (a) the total energy into the mixed layer from vertical entrainment during the freezing period, and as a function of (b) the mixed layer depth on the ice formation date, in each run of the 1D ensemble. The color of each dot indicates the date of the storm and its size its total momentum. The results for the reference and storm runs are shown with the red and black crosses, respectively.

Figure 9. Time series of the different contributions to the production of TKE for the reference and storm runs (red and cyan respectively) during (left) the open water period and (right) the freezing period: (a, b) heat and freshwater contributions (plain and dashed lines respectively) to the buoyancy-forced production of TKE (c, d) buoyancy-forced production of TKE, (e) mechanical-forced production of TKE (sum of W_d and W_s), (f) wind-forced production of TKE (g, h) ratio of buoyancy to mechanical-forced productions of TKE. The orange shadings indicate the period of the storm. The vertical red and cyan lines represent the ice formation dates in the reference and storm runs respectively.

Figure 10. (a) Initial temperature and salinity profiles (respectively red, bottom x-axis and blue, top x-axis) used in the NSS ensemble. The initial profiles used in the 1D ensemble are plotted in dashed lines for comparison. (b) Zoom on the top 80 m of the profiles shown in (a).

Figure 11. Same as Figure 3 but for the NSS case.

Figure 12. (a) Sea ice thickness maximum plotted as a function of the ice formation date in each run of the NSS ensemble. The size of each dot indicates the momentum of the storm. (b) Integrated mixed layer heat content during the open water period plotted as a function of storm momentum for each run of the NSS ensemble. For both panels, the color of each dot indicates the date of the storm. The results for the NSS reference and NSS storm runs are shown with the red and black crosses, respectively.

Figure 1.

Initial conditions

(a)

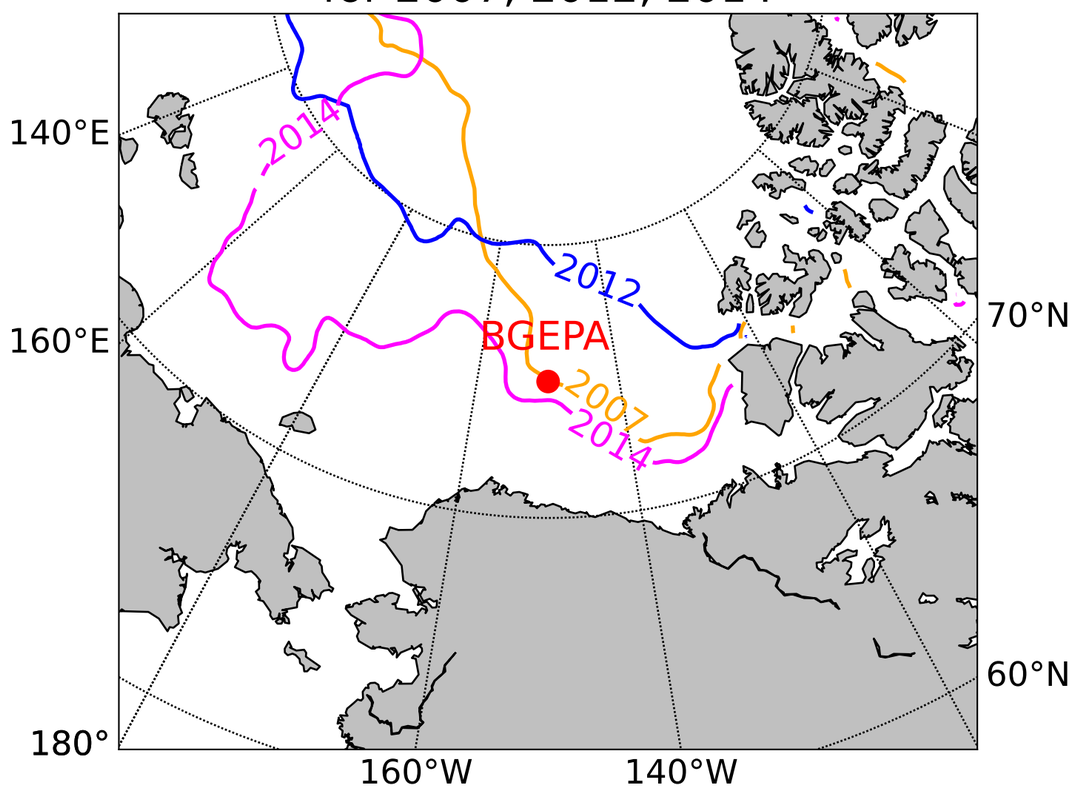

(b)

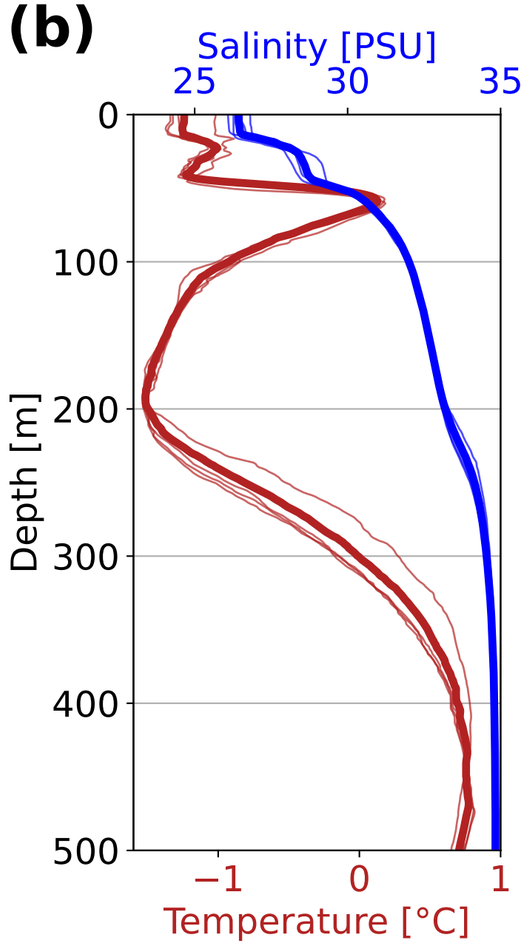

(c)

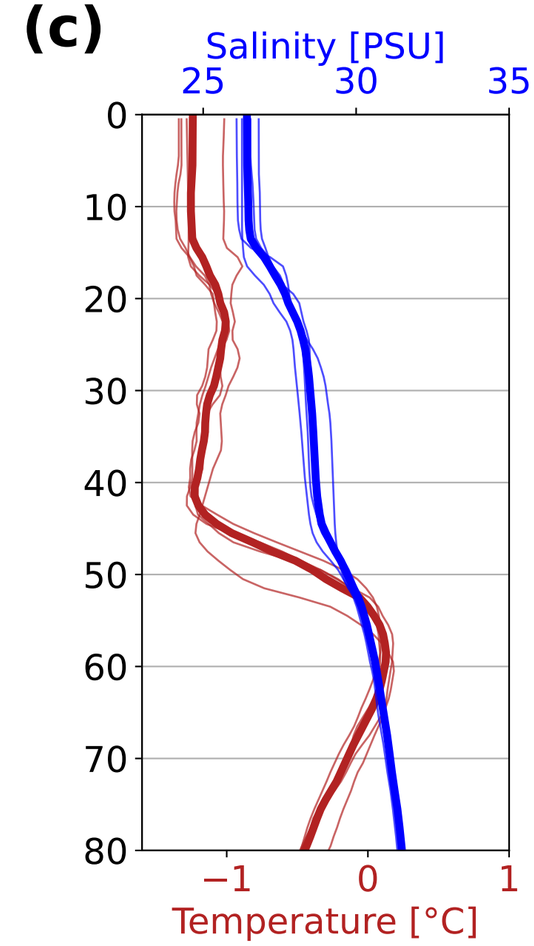

(d)

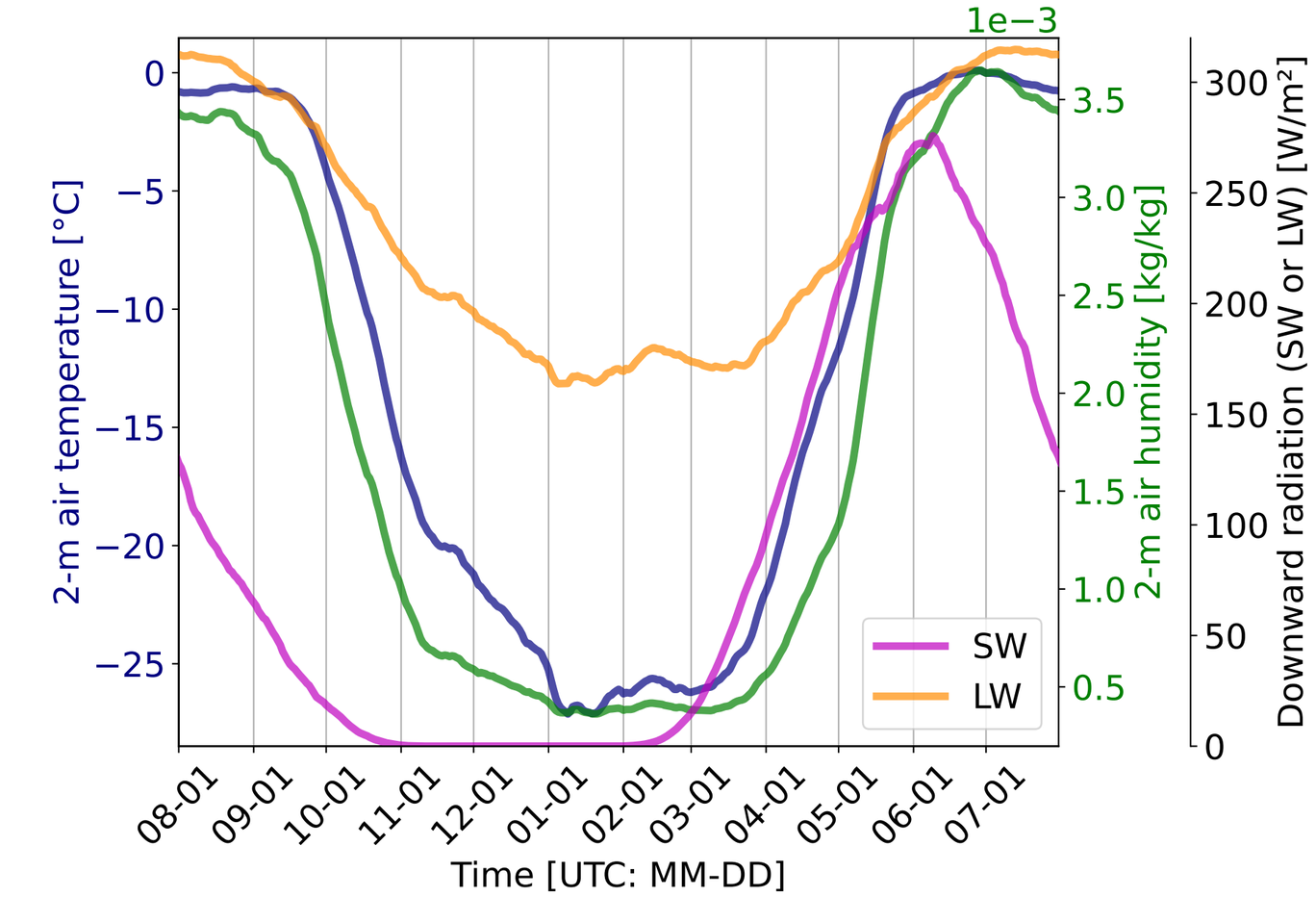

(e)

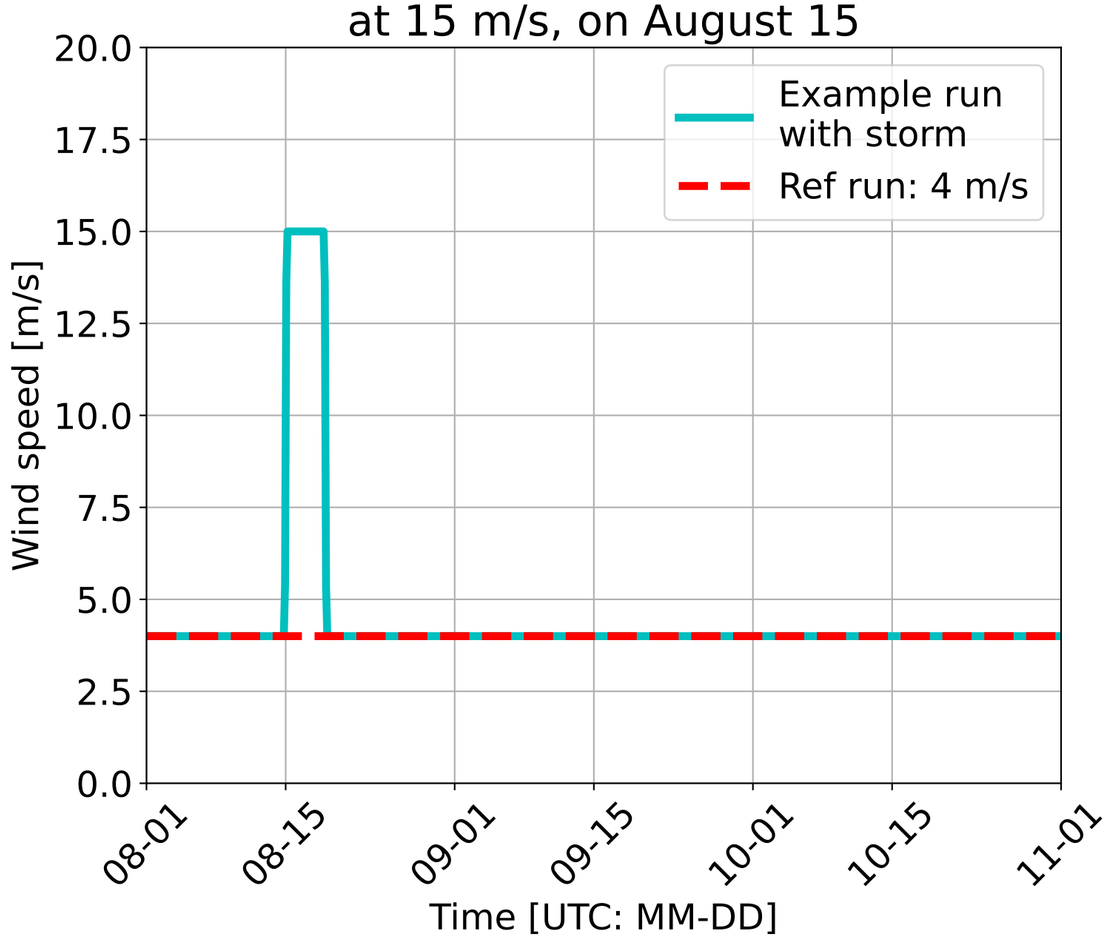

Figure 2.

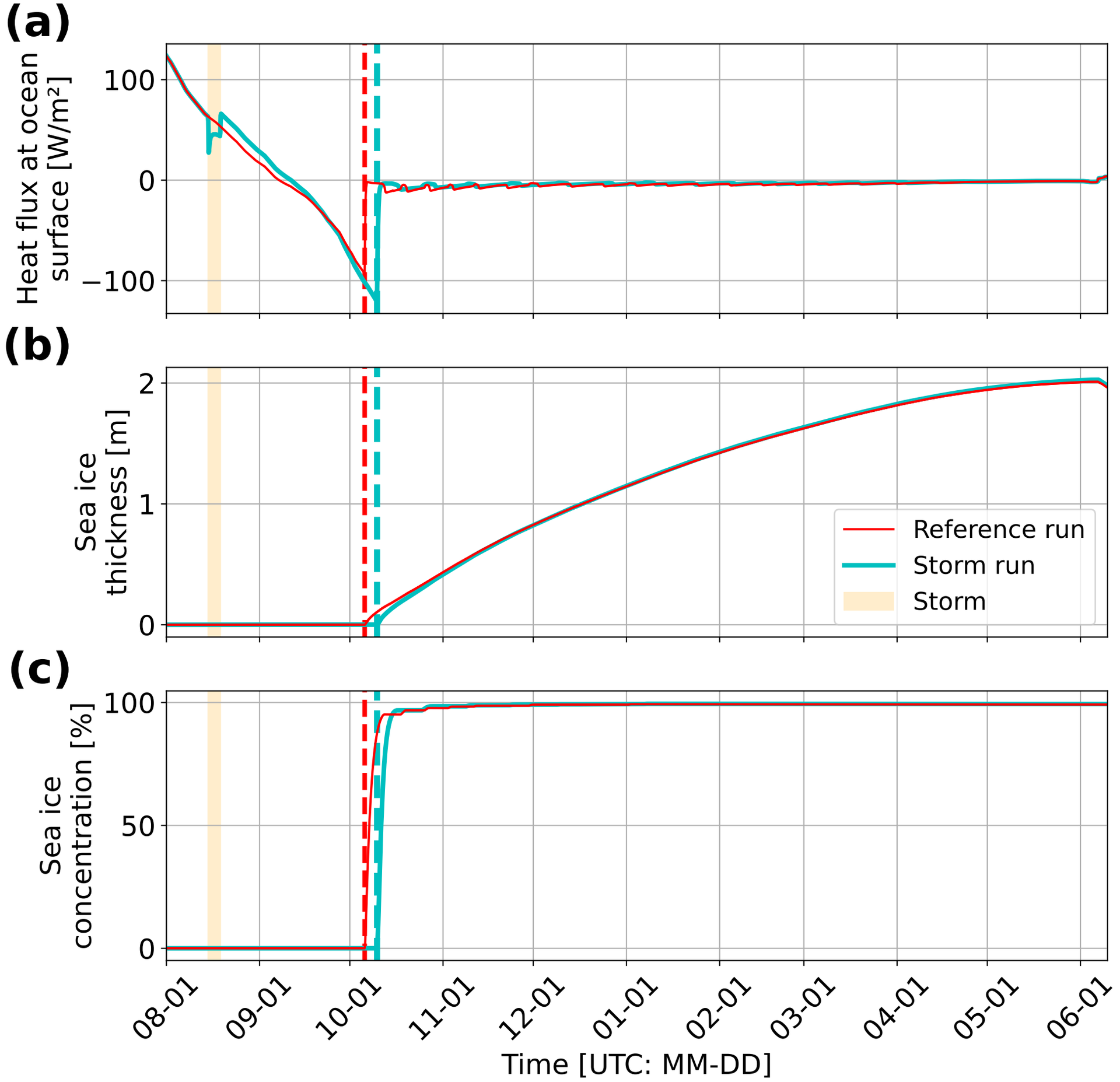
(a)
Heat flux at ocean surface [W/m²]
100
0
−100
(b)
Sea ice thickness [m]
2
1
0
Reference run
Storm run
Storm
(c)
Sea ice concentration [%]
100
50
0
08-01
09-01
10-01
11-01
12-01
01-01
02-01
03-01
04-01
05-01
06-01
Time [UTC: MM-DD]

Figure 3.

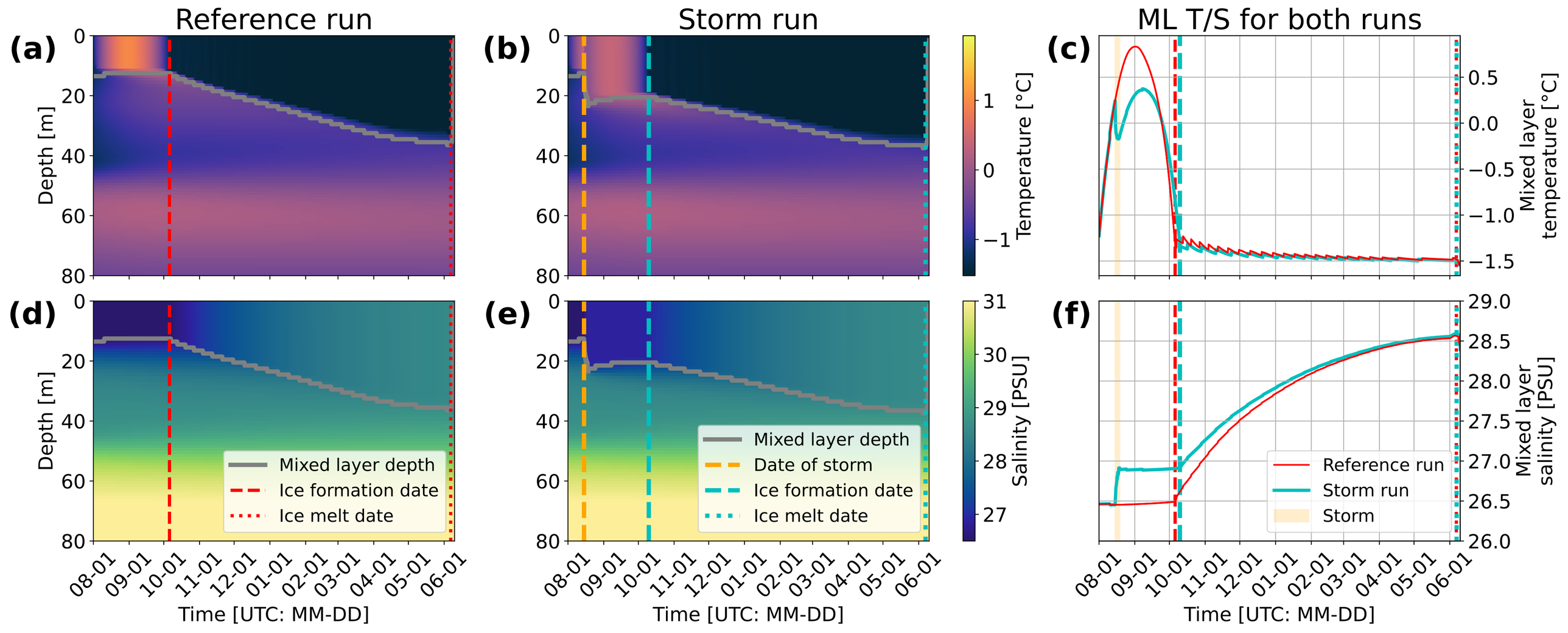
Reference run
Storm run
ML T/S for both runs
(a)
(b)
(c)
(d)
(e)
(f)
Depth [m]
Temperature [°C]
Mixed layer temperature [°C]
Salinity [PSU]
Mixed layer salinity [PSU]
Mixed layer depth
Ice formation date
Ice melt date
Date of storm
Reference run
Storm run
Storm
Time [UTC: MM-DD]
08-01
09-01
10-01
11-01
12-01
01-01
02-01
03-01
04-01
05-01
06-01

Figure 4.

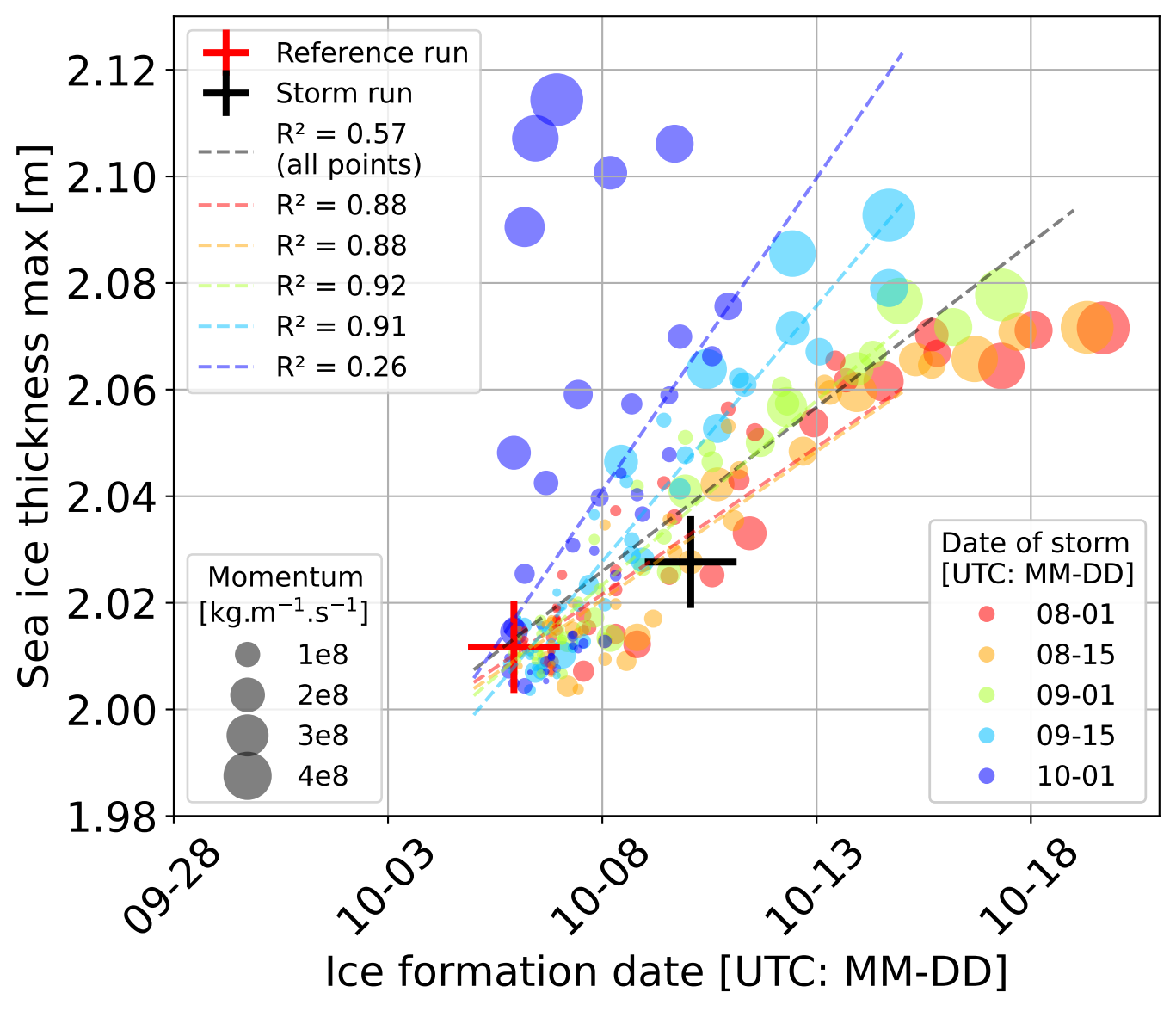
Reference run
Storm run
R² = 0.57
(all points)
R² = 0.88
R² = 0.88
R² = 0.92
R² = 0.91
R² = 0.26
Momentum
[kg.m⁻¹.s⁻¹]
1e8
2e8
3e8
4e8
Date of storm
[UTC: MM-DD]
08-01
08-15
09-01
09-15
10-01
Sea ice thickness max [m]
2.12
2.10
2.08
2.06
2.04
2.02
2.00
1.98
09-28
10-03
10-08
10-13
10-18
Ice formation date [UTC: MM-DD]

Figure 5.

Mixed layer temperature budget:
TOTAL

(a)

1e−6

Rate of change of mixed layer temperature [°C/s]

Change in mixed layer temperature [°C]

Mixed layer temperature

(b)

Mixed layer temperature [°C]

Reference run

Storm run

Storm

Mixed layer temperature budget:
DECOMPOSITION (3 terms below)

(c)

1e−6

Effect of surface heat flux [°C/s]

Cumulative effect of surface heat flux [°C]

Mixed layer freezing point temperature

(d)

Mixed layer freezing point temperature [°C]

(e)

1e−6

Effect of vertical entrainment [°C/s]

Cumulative effect of vertical entrainment [°C]

Mixed layer depth

(f)

MLD [m]

(g)

1e−6

Effect of vertical diffusion [°C/s]

Cumulative effect of vertical diffusion [°C]

Mixed layer heat content

(h)

1e8

Mixed layer heat content [J/m²]

08-01

08-15

09-01

09-15

10-01

Time [UTC: MM-DD]

Figure 6.

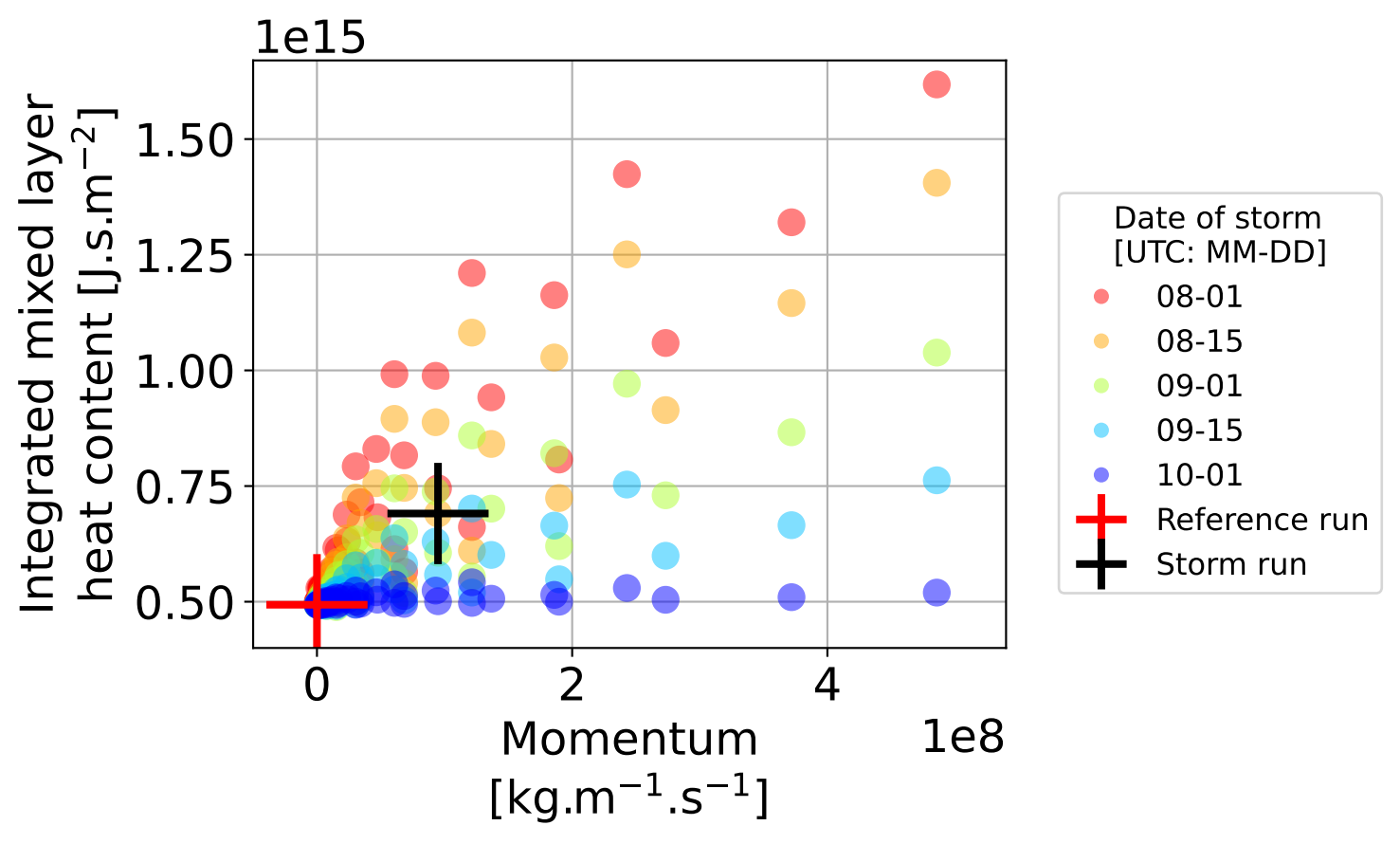
1e15
1.50
1.25
1.00
0.75
0.50
Integrated mixed layer heat content [J.s.m^{-2}]
0
2
4
1e8
Momentum [kg.m^{-1}.s^{-1}]
Date of storm [UTC: MM-DD]
08-01
08-15
09-01
09-15
10-01
Reference run
Storm run

Figure 7.

(a)

Sea ice thickness difference [m]

0.1
0.0
−0.1

Storm - reference run

(b)

MLD [m]

0
10
20
30

Reference run
Storm run

(c)

1e−6

Effect of vertical entrainment [°C/s]

0
2
4

Cumulative effect of vertical entrainment [°C]

0.00
0.25
0.50
0.75
1.00

(d)

Surface temperature [°C]

−1.40
−1.45
−1.50
−1.55

T_{FP_s} in reference run
T_{FP_s} in storm run

10-01
11-01
12-01
01-01
02-01
03-01
04-01
05-01
06-01

Time [UTC: MM-DD]

Figure 8.

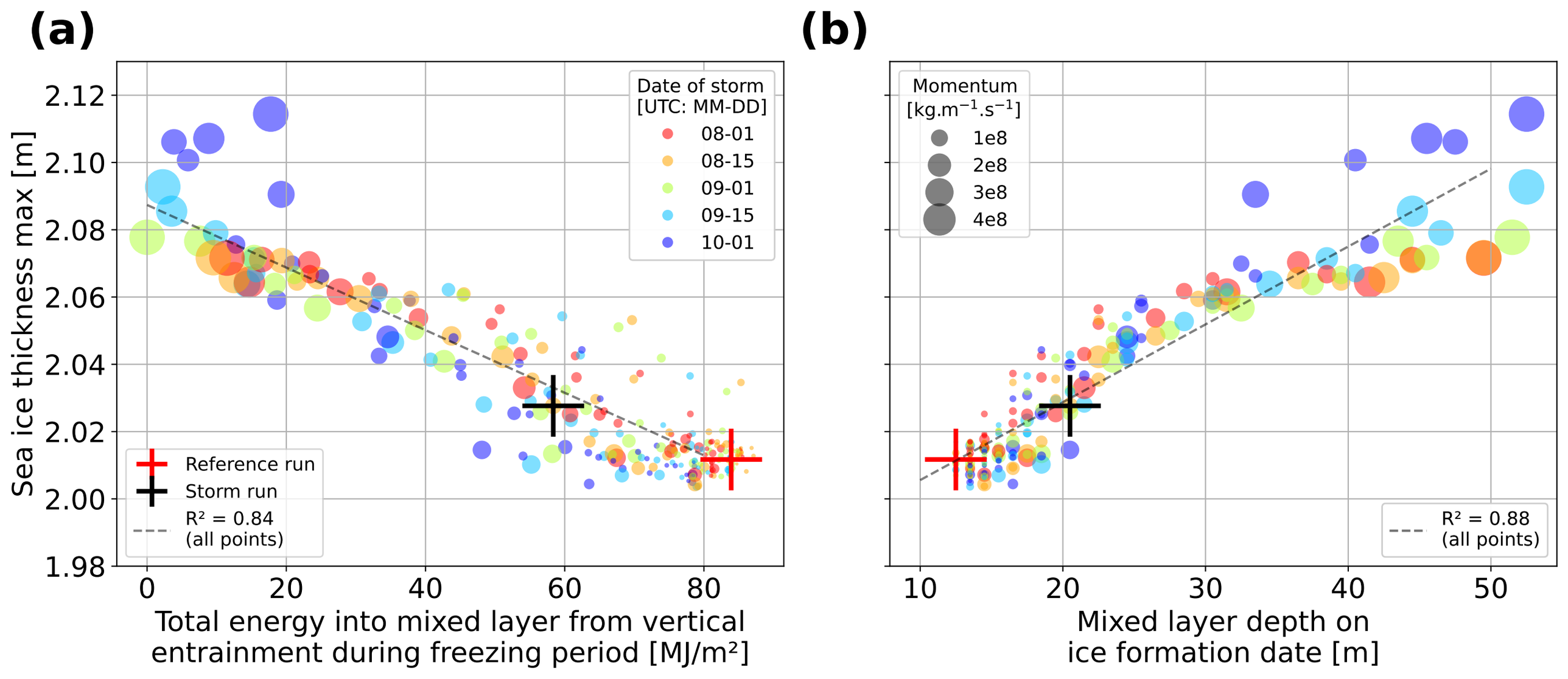
(a)
(b)
Sea ice thickness max [m]
2.12
2.10
2.08
2.06
2.04
2.02
2.00
1.98
0
20
40
60
80
Total energy into mixed layer from vertical entrainment during freezing period [MJ/m²]
Date of storm [UTC: MM-DD]
08-01
08-15
09-01
09-15
10-01
Reference run
Storm run
R² = 0.84 (all points)
Momentum [kg.m⁻¹.s⁻¹]
1e8
2e8
3e8
4e8
R² = 0.88 (all points)
10
20
30
40
50
Mixed layer depth on ice formation date [m]

Figure 9.

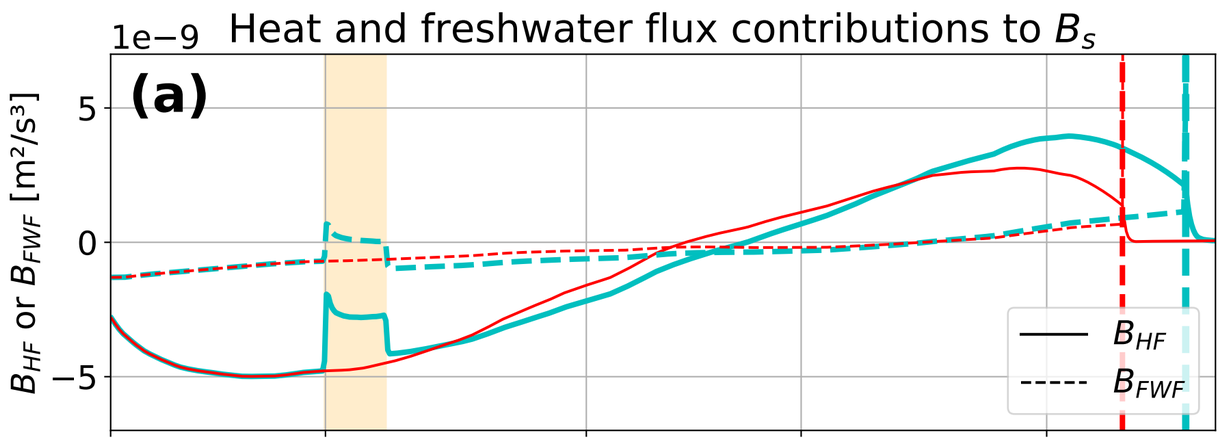
Heat and freshwater flux contributions to B_s
1e−9
(a)
B_{HF} or B_{FWF} [m²/s³]
B_{HF}
B_{FWF}

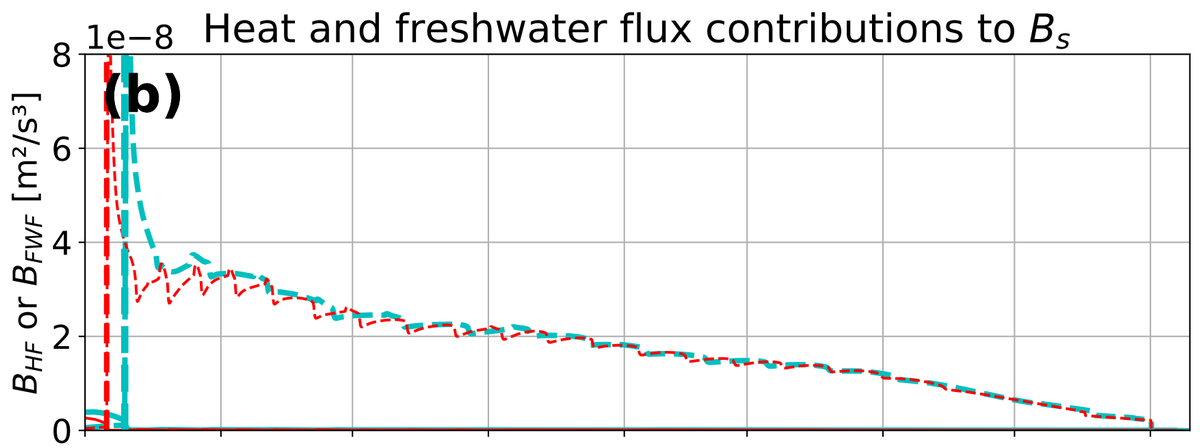
Heat and freshwater flux contributions to B_s
1e−8
(b)
B_{HF} or B_{FWF} [m²/s³]

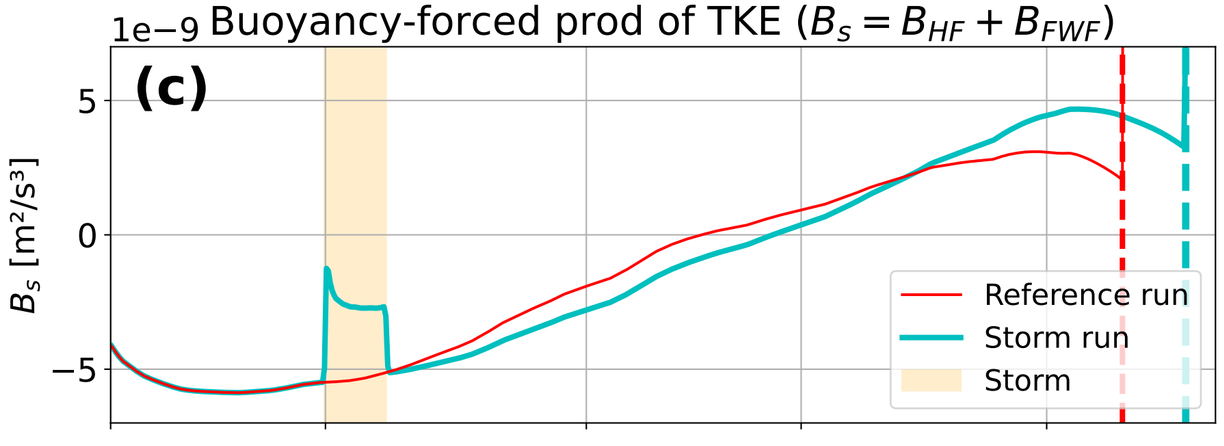
Buoyancy-forced prod of TKE ($B_s = B_{HF} + B_{FWF}$)
1e−9
(c)
B_s [m²/s³]
Reference run
Storm run
Storm

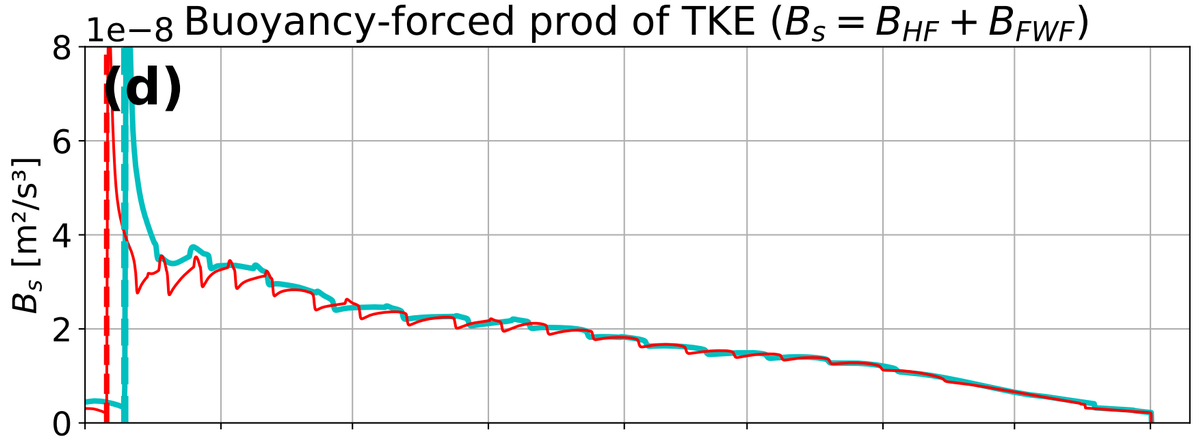
Buoyancy-forced prod of TKE ($B_s = B_{HF} + B_{FWF}$)
1e−8
(d)
B_s [m²/s³]

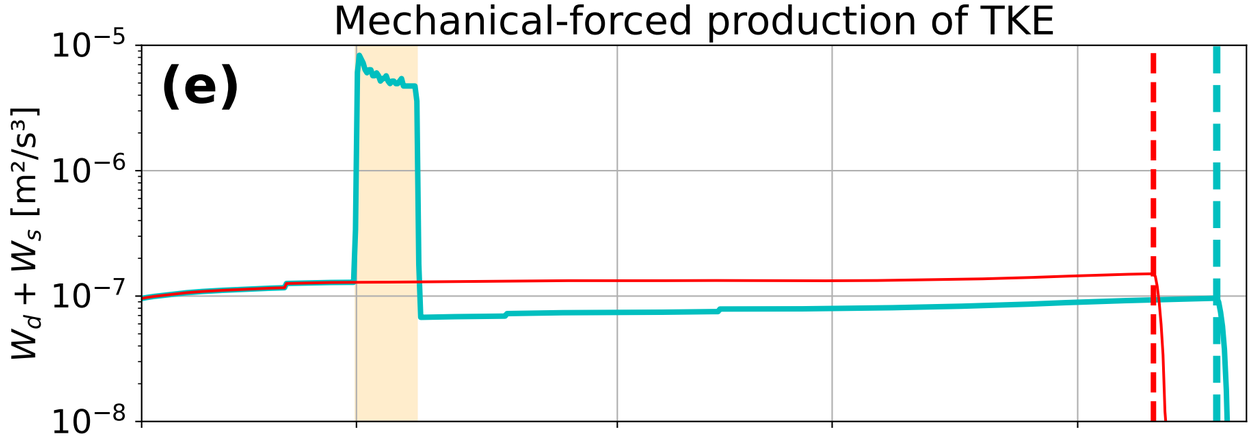
Mechanical-forced production of TKE
(e)
$W_d + W_s$ [m²/s³]

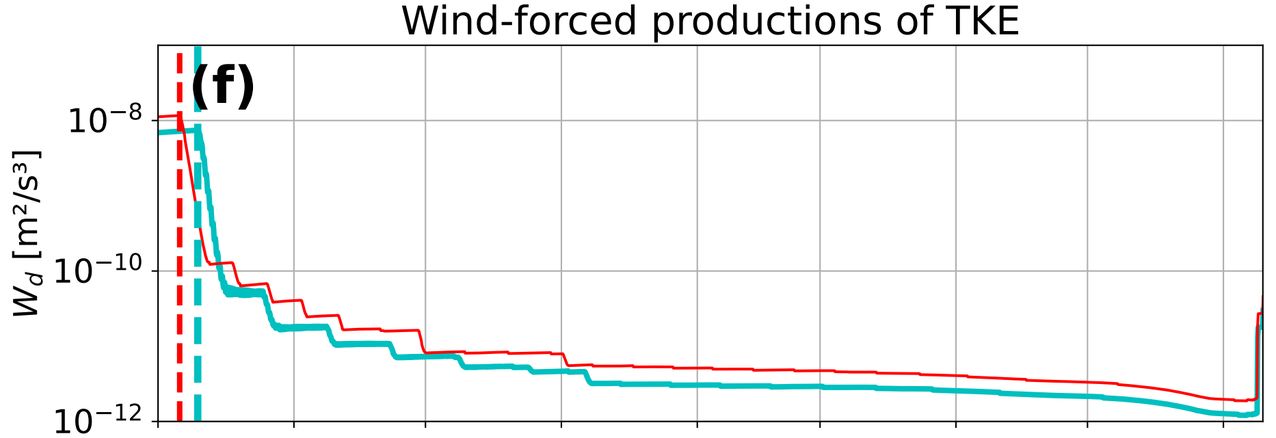
Wind-forced productions of TKE
(f)
W_d [m²/s³]

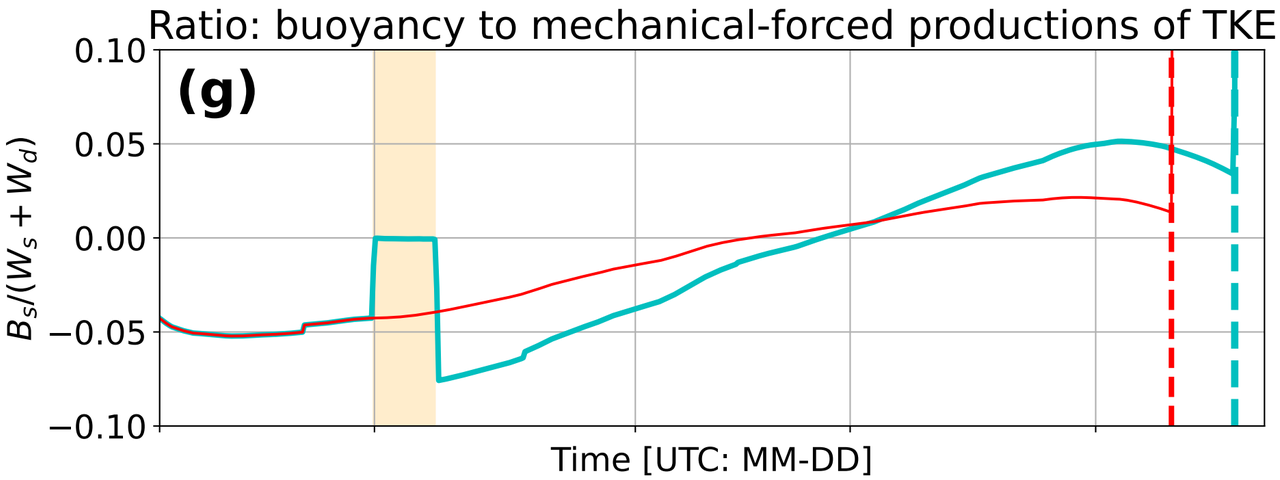
Ratio: buoyancy to mechanical-forced productions of TKE
(g)
$B_s/(W_s + W_d)$
Time [UTC: MM-DD]

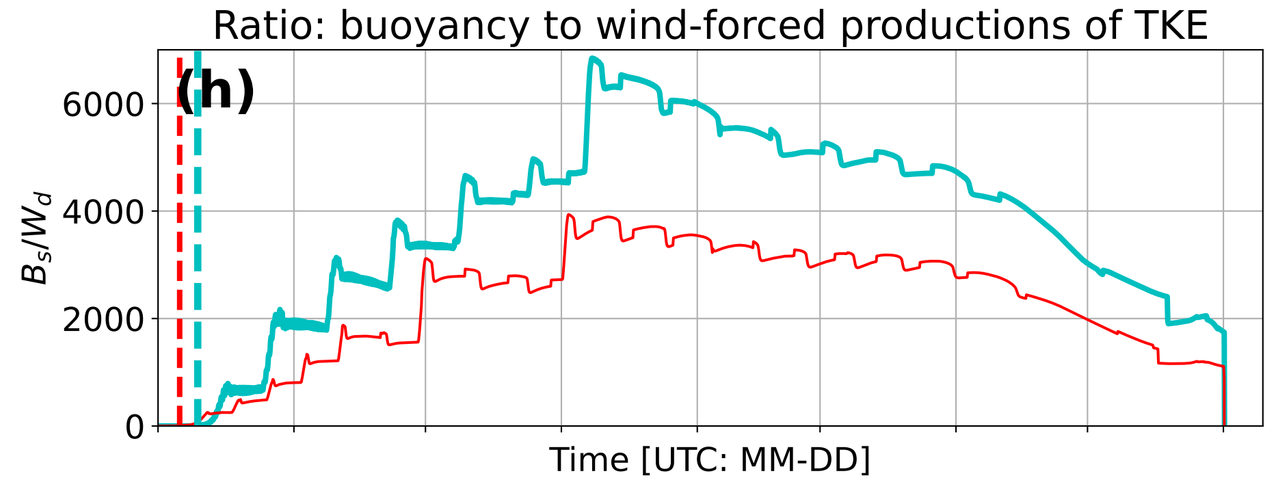
Ratio: buoyancy to wind-forced productions of TKE
(h)
B_s/W_d
Time [UTC: MM-DD]

Figure 10.

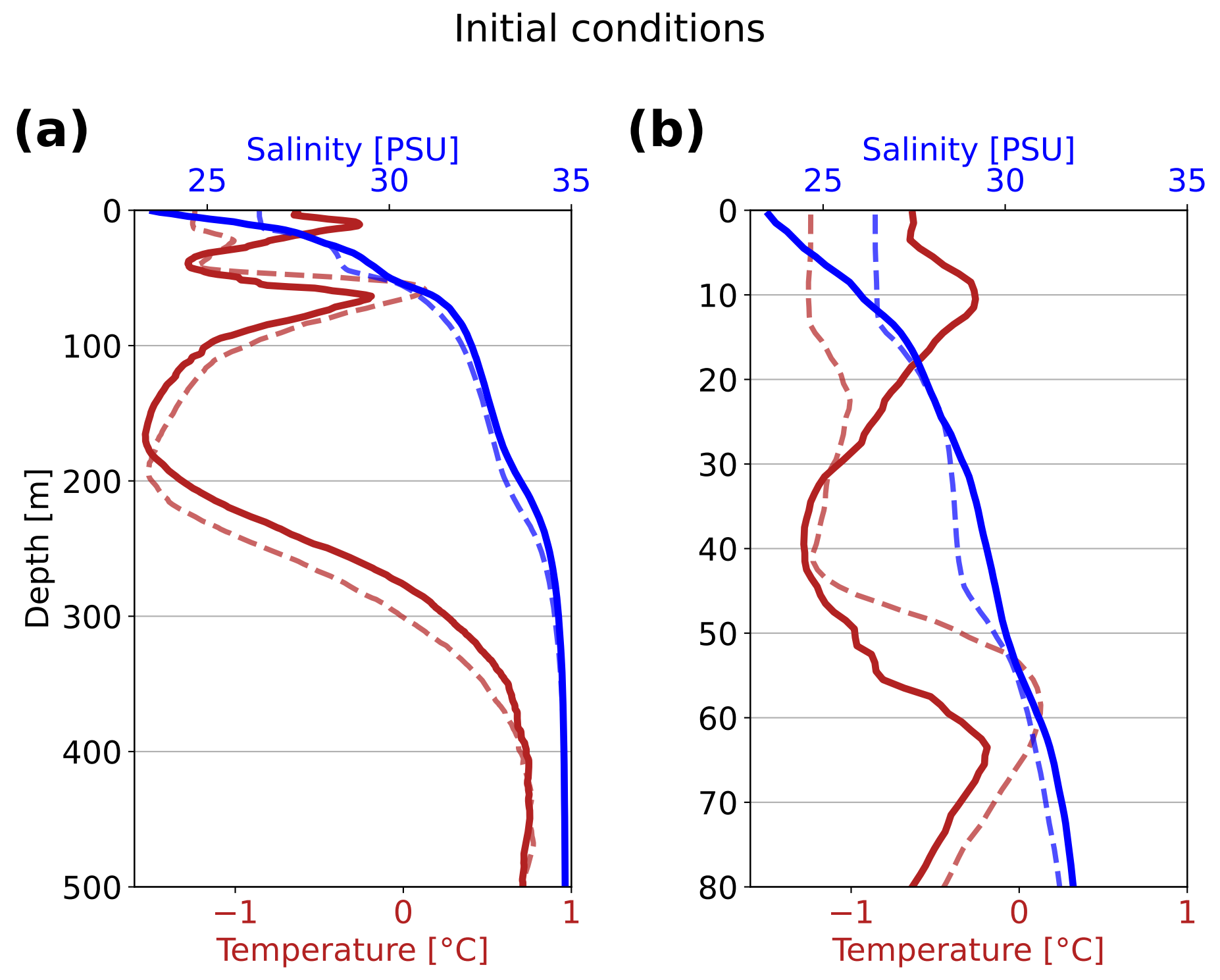
Initial conditions
(a)
Salinity [PSU]
25
30
35
0
100
200
300
400
500
Depth [m]
−1
0
1
Temperature [°C]
(b)
Salinity [PSU]
25
30
35
0
10
20
30
40
50
60
70
80
−1
0
1
Temperature [°C]

Figure 11.

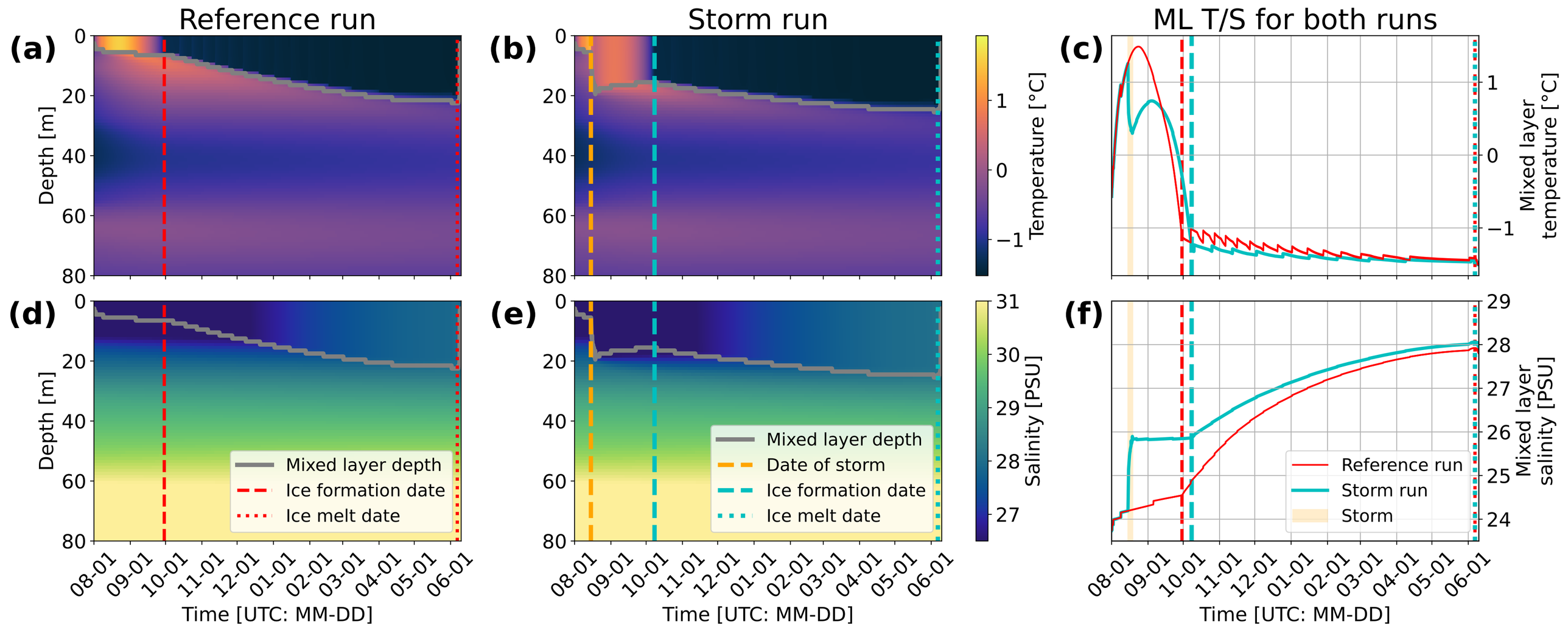
Reference run
Storm run
ML T/S for both runs
(a)
(b)
(c)
(d)
(e)
(f)
Depth [m]
Temperature [°C]
Mixed layer temperature [°C]
Salinity [PSU]
Mixed layer salinity [PSU]
Time [UTC: MM-DD]
Mixed layer depth
Ice formation date
Ice melt date
Date of storm
Reference run
Storm run
Storm
08-01
09-01
10-01
11-01
12-01
01-01
02-01
03-01
04-01
05-01
06-01

Figure 12.

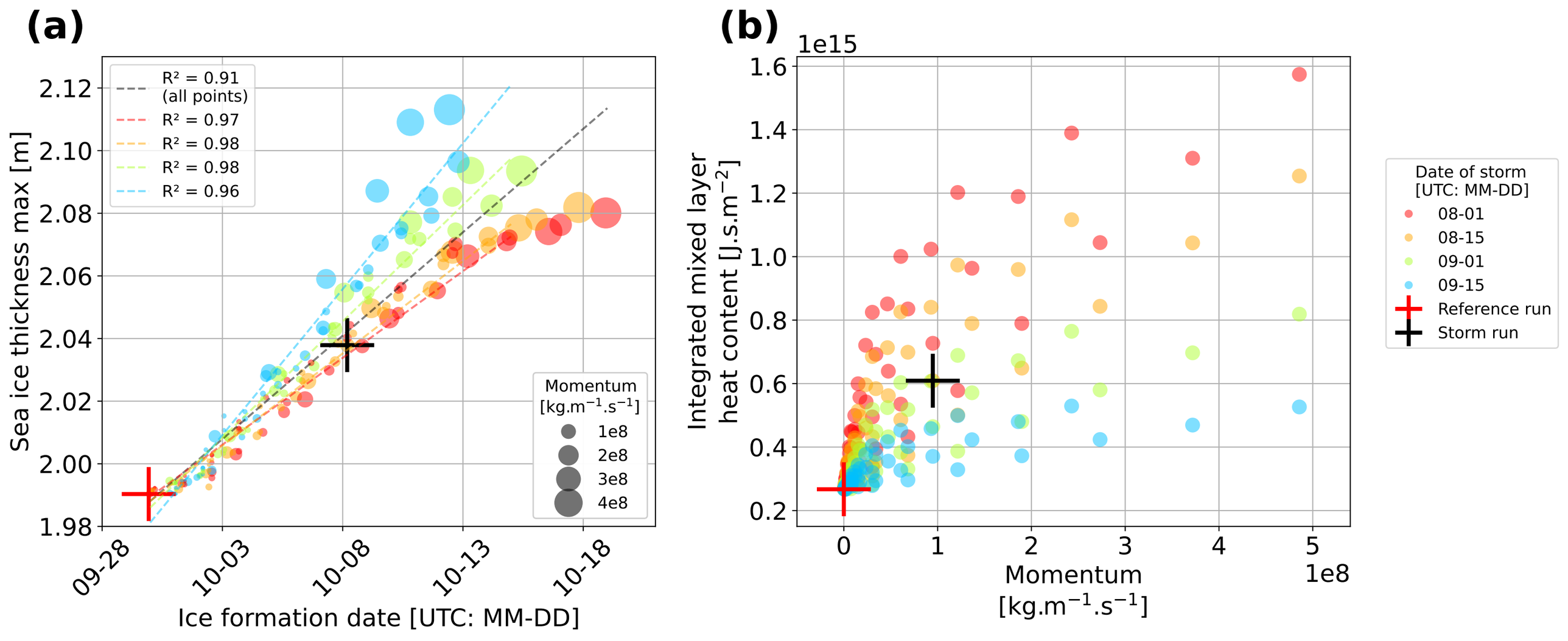
(a)
R² = 0.91
(all points)
R² = 0.97
R² = 0.98
R² = 0.98
R² = 0.96
Momentum
[kg.m⁻¹.s⁻¹]
1e8
2e8
3e8
4e8
Sea ice thickness max [m]
2.12
2.10
2.08
2.06
2.04
2.02
2.00
1.98
09-28
10-03
10-08
10-13
10-18
Ice formation date [UTC: MM-DD]
(b)
1e15
Integrated mixed layer
heat content [J.s.m⁻²]
1.6
1.4
1.2
1.0
0.8
0.6
0.4
0.2
0
1
2
3
4
5
1e8
Momentum
[kg.m⁻¹.s⁻¹]
Date of storm
[UTC: MM-DD]
08-01
08-15
09-01
09-15
Reference run
Storm run